

New Data Analysis and Visualization Methods for Ultrafast Electron Diffraction

Laurent P. René de Cotret

Department of Physics
McGill University
Montréal, Quebec, Canada
December 7, 2016

A thesis submitted to McGill University
in partial fulfillment of the requirements of the degree of
Master of Science

© Laurent P. René de Cotret, 2016

TABLE OF CONTENTS

List of Figures	4
Abstract	9
Résumé	10
Acknowledgments	11
Introduction	12
References	13
1 Structural Dynamics in Vanadium Dioxide	15
1.1 The Phases of Vanadium Dioxide	16
1.2 Two Theoretical Models of the Insulator-Metal Transition of VO ₂	17
1.2.1 Peierls Distortions and The Goodenough Model	18
1.2.2 Strong Electronic Correlations and the Mott-Hubbard Model	20
1.3 Simulations Studies	21
1.4 Insulator-Metal Transition via Ultrafast Photoexcitation	22
References	23
2 Electron Diffraction Formalism	27
2.1 Scattering	27
2.2 Scattering in Crystals: Diffraction	28
2.2.1 Structure Factors	29
2.2.2 Visualizing Diffraction Conditions with the Ewald Sphere	29
2.3 Scattering Potential Maps	31
2.4 The Patterson Function	32
2.5 Addendum: Sensitivity to Atomic Form Factor Changes	32
References	33

3	Data Acquisition and Processing	35
3.1	Experimental Setup	35
3.1.1	Overview	35
3.1.2	Laser System	36
3.1.3	Electron Beam Generation	38
3.1.4	Radio-frequency Compression of Electron Bunches	39
3.1.5	Sample Chamber	39
3.1.6	Detection	40
3.2	Data Acquisition and Processing	41
3.2.1	Acquisition Procedure	41
3.2.2	Image Processing	41
3.3	Polycrystalline Texture	43
3.3.1	Orientation Data	43
3.3.2	Texture Correction via Pole Density	45
3.4	Baseline Determination Using the Discrete Wavelet Tranform	46
3.4.1	The Discrete Wavelet Transform	47
3.4.2	An Iterative Algorithm	49
3.4.3	Testing via simulations	49
	References	50
4	Scattering Potential Maps and a Photoinduced Metal-like Phase of VO ₂	54
4.1	From Data to Scattering Potential Maps	54
4.1.1	Diffracted Intensity	55
4.1.2	Diffraction Phase from Structure Factors	55
4.2	Testing on Static Diffraction Data	56
4.2.1	Comparison of Radial Pair-distribution Functions	57
4.3	A Photoinduced Metal-like Phase of Monoclinic VO ₂	60
4.4	The Structure of the Photoinduced Monoclinic Metal-like State of VO ₂ via Scattering Potential Maps	62
4.5	Discussion with a Theoretical Perspective	64
	References	67
	Conclusion	69
	Outlook	70
	References	70
A	Structural Parameters of VO ₂ Crystal Phases	72

List of Figures

<u>Figure</u>	<u>page</u>
1–1 Crystallographic structure of VO ₂ . Oxygen atoms (green) form an octahedral cage (green overlay) around vanadium atoms (blue). Top: 3/2 unit cells of the insulating, low-temperature monoclinic M1 structure. Bottom: two unit cells of the metallic, high-temperature rutile structure. Figure adapted with permission from [6].	17
1–2 Graphical representation of the e _g and t _{2g} orbitals. e _g orbitals are labeled d _{3z²-r²} (a) and d _{xy} = d (b). t _{2g} orbitals are labeled d _{x²-y²} (c), d _{xz} (d) and d _{yz} (e). Figure adapted with permission from [7].	19
1–3 Diagram of the V 3d orbitals splitting between the monoclinic M1 and rutile structures of VO ₂ [9].	20
1–4 Diagram of the localized and delocalized electron states in a lattice. Top: localized electrons in a high lattice potential give rise to an insulating behaviour in VO ₂ . Bottom: Low lattice potential favours delocalized electrons, which in turn increase conductivity but can result in multiple electron occupancy at each vanadium site. [10].	21
2–1 Elastic scattering experiments measure the diffracted intensity at wavevectors G (red) where the Ewald sphere (blue, dashed) coincides with the reciprocal lattice.	30
2–2 Left: x-ray form factor of Cu. Electron diffraction is more sensitive to valence charge distribution changes than X-ray diffraction in the regions where $f^x(s) > Z/2$ ($s_c = 0.47 \text{ \AA}^{-1}$). Right: contribution of individual electron orbital to the X-ray form factor of Cu [5].	33

3–1	Diagram of the ultrafast electron diffractometer. An oscillator drives both a laser amplifier and a phase-lock loop. The laser beam is split between a pump and a probe, while the phase-lock loop synchronizes an amplified RF cavity to the pump and probe beams. The RF cavity acts as a temporal lens to focus the probe electron beam onto the sample.	36
3–2	High voltage electron accelerator design rated up to 100 kV. Macor parts (white) support the cathode structure, and stainless steel (hatched) is used to shield Macor from emitted electrons. Figure adapted with permission from [3]	38
3–3	Schematic of the radio-frequency electron compression cavity presented by Van Oudheusden et al. [2]. Figure adapted with permission from [3]	40
3–4	Top left: raw diffraction image of a polycrystalline sample of VO ₂ before photoexcitation. Top right: Raw diffraction image of polycrystalline sample of VO ₂ , with Debye-Scherrer rings fit, as well as beamblock mask. Bottom: radial average, showing a low-frequency background, as well as elastic scattering peaks.	42
3–5	Texture data taken from the VO ₂ sample used in this work. Top: SEM image of the sample surface, showing crystallite sizes. Bottom: spacial distribution of crystallite normals, computed from EBSD data, separated into Euler angles E1, E2, and E3 (left to right).	44
3–6	Distribution of crystallite normal directions (pole [100]) of a VO ₂ sample using angular data from Fig. 3–5 uncorrected for crystallite area. The distribution shows the presence of preferred orientations.	45
3–7	Pole density for the VO ₂ sample used in this work. A pole density higher than unity signifies an over-represented scattering vector orientation.	46
3–8	Diagram of the Mallat algorithm for the multi-level discrete wavelet transform. The original signal (left, green) is decomposed into a set of approximate coefficients (top, blue) and a set of detail coefficients (bottom, yellow) . Further decomposition levels are iteration of the previous procedure on the approximate coefficients.	48
3–9	Effect of iteration in baseline determination on real data. The algorithm converges quickly to a baseline.	50
3–10	Simulated experiment showcasing a phase transition of VO ₂ from monoclinic M1 (purple) to rutile (red). The phase transition speed has an exponential time constant of 200 fs. A static background is added.	51

3–11 Top: baseline-subtracted diffraction patterns from Fig. 3–10. Characteristic peaks of the phase transition are highlighted by black lines. The time-constant of the intensity change at those characteristic peaks averages (200 ± 20) fs, in agreement with the simulation parameter of 200 fs. Bottom: residuals between the known diffraction patterns and their reconstruction.	51
4–1 Electron diffraction data for polycrystalline sample of VO_2 , averaged over times before photoexcitation.	57
4–2 Scattering potential map of equilibrium monoclinic M1 VO_2 . Both maps intersect at the red dashed line. Linear cuts are taken to highlight features. Top: scattering potential map cutting through the V – V dimers (blue overlay), characteristic of the monoclinic M1 VO_2 crystal structure. Two non-equivalent orientations of the oxygen octahedra are shown in red overlay. Bottom: scattering potential map perpendicular to the vanadium dimers. The oxygen octahedra (red overlays) are all oriented in the same direction	58
4–3 Left: average radial pair-distribution function $G(r, t)$ of times before photoexcitation, computed in two ways from the same data. Highlighted extrema represent inter-atomic distances shown on the right. Right: monoclinic M1 structure of VO_2	59

4–4 Structural dynamics during the insulator-metal transition in VO₂.
A: Background-subtracted ultrafast electron diffraction data from 0 to 20 ps. Red vertical lines indicate some reflections that are allowed in the M1 structure, but not in R. Blue vertical lines indicate reflections that are allowed in both M1 and R. Gray vertical lines indicate peaks that are associated with the crystallographic direction perpendicular to \mathbf{c}_R (\mathbf{a}_M).
B: Difference diffraction pattern from -0.5 to 20 ps. **C:** Time-resolved diffraction peak intensity showing fast (310 fs) and slow (1.6 ps) dynamics, respectively, for peaks indicated by red and blue vertical lines in (A), (B), (E), and (F). **D:** Fluence dependent of the fast and slow signal amplitudes as measured from (30̄2) and (220) peaks shown in (C). The range of fluences for which no phase transition is observed is indicated by hatched region. Inset: time-resolved IR (5 μm, 0.25 eV) transmissivity in the hatched fluence region displays a persistent decrease to a very long-lived plateau (>100 ps). The amplitude of this decrease reaches > 99% at 3.7 mJ cm⁻², indicating a closing of the semiconducting gap and a transition to a metallic-like state.
E: Difference diffraction pattern for fast dynamics, showing nonthermal melting of the M1 structure into rutile. **F:** Difference diffraction pattern for slower dynamics, showing no changes in crystallographic structure. Between 3 and 9 mJ cm⁻² pump fluence, only these changes are observed. Figure reproduced from [1] with permission. **F:** Diffraction difference spectrum for the slow dynamics. The change in diffracted intensity from 2 to 10 ps (referenced to 2 ps) is shown. Figure reproduced with permission from [1].

61

4–5 Electrostatic potential map computed from difference intensity data of 10 ps (referenced at 2 ps). The planes are equivalent orientations to Fig. 4–2. Both vanadium and oxygen atoms grow more positive as the electrons move to reinforce the charge-density wave. Changes in the electrostatic potential follows an anti-ferroelectric pattern, highlighted by arrows. **Top:** difference electrostatic potential along the oxygen plane. **Bottom:** difference electrostatic potential along the unit cell floor, oriented along the solid red line through the page.

63

4–6 Change in the radial pair-distribution function $\Delta G(r, t) = G(r, 10 \text{ ps}) - G(r, 2 \text{ ps})$. Highlighted extrema represented inter-atomic distances shown on Fig. 4–3.

64

4–7 Energy landscape of monoclinic VO₂ at different values of U and with $V = 1 \text{ eV}$ fixed, as a function of d_{xz} orbital occupancy. A local minima corresponding to a metallic metastable state is present for $U \geq 4.5 \text{ eV}$. Reproduced from [6] with permission.

65

- 4–8 **Left:** simulated partial energy band diagram of the equilibrium (insulating) monoclinic M1 VO_2 phase. **Right:** simulated partial energy band diagram of the metastable phase of VO_2 ($U = 4.5 \text{ eV}$, $V = 1 \text{ eV}$) shows no gap at the Fermi level. Reproduced from [6] with permission. 66
- 4–9 Energy gap E_{gap} as a function of energy injected per unit cell by the laser pulse under various parameters U and V . Adapted from [6] with permission. 67

Abstract

In this thesis, a computational techniques for visualizing crystalline electrostatic potential on the femtosecond time-scale is presented. This technique, called *scattering potential mapping*, displays local information on lattice changes and charge-density reorganization over time from ultrafast electron diffraction data. It can be applied directly on diffraction intensities from previous experiments. This tool is consistent with previous results, most importantly with radial pair-distribution function analyses. Scattering potential mapping could lead to easier comparison between experiments and simulations.

A baseline-removal routine built on the discrete wavelet transform is also detailed in this work, as a replacement for the unstable interpolation and curve-fitting techniques typically used. This routine perfectly reconstructs structural dynamics, as measured via diffraction, in simulations.

Résumé

Cette thèse décrit une technique d'analyse permettant la visualisation de la dynamique du champ electrostatique à l'échelle de la femto-seconde. Cette technique, appelée *imagerie du potentiel de diffusion*, exhibe de l'information local sur les changements de structure et la réorganisation électronique d'un treillis d'atome, provenant de données de diffraction par électron ultrarapide. Cet outil est cohérent avec de précédentes analyses, utilisant notamment des distribution de paires. L'imagerie du potentiel de diffusion pourra permettre de mieux comparer les résultats d'expériences et de simulations.

Un programme de soustraction de fond, utilisant la transformée en ondelette discrète, est aussi présenté. Cet algorithme remplace les techniques basées sur l'interpolation et l'ajustement de courbes, techniques instables typiquement utilisées dans le domaine.

Acknowledgements

The techniques and results described in this thesis could not have come to fruition without the work of many.

The author thanks colleagues Mark J. Stern, Martin R. Otto and Jean-Philippe Boisvert and thesis advisor Bradley J. Siwick for their support and help in learning the ropes of ultrafast electron diffraction and writing this thesis.

The in-house software written based on techniques developed in Chapter 3 and Chapter 4 is built on top of the scientific Python software stack known as SciPy. The low-level considerations were taken care of by a talented team of volunteers, so that the author was free to concentrate on the algorithms rather than software engineering implementations.

All code used herein is open-source and available on demand.

Introduction

Ultrafast electron diffraction is a novel technique that can resolve femtosecond-scale lattice and electronic dynamics. Data analysis techniques for ultrafast electron diffraction are, in principle, similar to ultrafast x-ray diffraction techniques. However, software analysis in ultrafast electron diffraction trails behind the X-ray field in terms of structure solving [1, 2], compensating for polycrystalline texture [3, 4] and subtracting inelastic scattering background [5], for example.

The goal of this work is to develop a suite of techniques for analysing and exploring structural and electronic dynamics that are contained in ultrafast electron diffraction data. The first technique, called scattering potential mapping, provides a real-space representation of the structural and electronic dynamics in a crystalline sample. The second tool is a new iterative baseline-removal technique based on the discrete wavelet transform, and exploration of the polycrystalline texture from electron back-scatter diffraction data.

Vanadium dioxide (VO_2) is used as a test system for the scattering potential maps. Chapter 1 gives a brief literature review on the structural dynamics associated with the insulator-metal transition in VO_2 , both proposed and measured. Chapter 2 introduces the formal basis of scattering potential maps, by summarizing the theory of scattering and electron diffraction. Chapter 3 describes the experimental setup used to acquire the data that

will be used in later chapters, and also details data processing, including a new background-removal technique based on the discrete wavelet transform. Chapter 4 goes over the computational techniques involved in the calculation of the scattering potential maps, as well as initial tests on equilibrium diffraction data from recent experiments. A recent publication by Morrison et al. [6], in which ultrafast electron diffraction on VO₂ revealed a new metastable phase, is then extended to show how scattering potential maps can be used to provide a much more detailed visualization of the structure of this metastable phase, while being fully consistent with earlier results.

References

- [1] Armel Le Bail. Whole powder pattern decomposition methods and applications: A retrospection. *Powder Diffr.*, 20(04):316–326, 2005.
- [2] W .I. F. David and K. Shankland. Structure determination from powder diffraction data. *Acta crystallographica. Section A, Foundations of crystallography*, 64(Pt 1):52–64, 2008.
- [3] W. A. Dollase. Correction of Intensities of Preferred Orientation in Powder Diffractometry: Application of the March Model. *Journal of Applied Crystallography*, 19(pt 4):267–272, 1986.
- [4] M. Jarvinen. Application of symmetrized harmonics expansion to correction of the preferred orientation effect. *Journal of Applied Crystallography*, 26(pt 4):525–531, 1993.
- [5] Fengkui Zhao and Aimin Wang. A background subtraction approach based on complex wavelet transforms in EDXRF. *X-Ray Spectrometry*, 44(2):41–47, 2015.
- [6] Vance R. Morrison, Robert P. Chatelain, Kunal L Tiwari, Ali Hendaoui, Andrew Bruhacs, Mohamed Chaker, and Bradley John Siwick. A photoinduced metallic phase of monoclinic VO₂ revealed by ultrafast electron diffraction. *Science*, 341(6208):19, 2014.

CHAPTER 1

Structural Dynamics in Vanadium Dioxide

Vanadium dioxide (VO_2) is part of the family of compounds known as the transition metal oxides. These compounds are of interest because of their wide range of applications, for example as dielectrics, semiconductors, as well as magnetic and optical uses. In particular, VO_2 stars as the poster child for an assortment of strongly-correlated materials with coupled orbitals and lattice instabilities.

VO_2 is a condensed matter physics playground due to the variety of (crystalline) phases it displays with widely-varying electronic, optical, and magnetic properties [1]. This material has been studied for over forty years, since the discovery of its thermal insulator-metal transition by Morin [2]. VO_2 is also of practical interest as thermochromic window coating [3] and in light-active electronics [4].

Despite decades of research on the phase transitions of VO_2 , the field is as active as ever. There are two competing views on the cause of the insulator-metal transition. While lattice distortions are thought to play a role, strong electronic correlations must also be considered. To this day, there is no consensus on the hierarchy of these two phenomenon. This section will provide context on the debate, which will be continued in Chapter 4.

The first section details the structural differences between those phases. The thermal insulator-metal transition is introduced next. This leads to the nonthermal insulator-metal transition accessed by ultrafast photoexcitation. Finally, for reference, a crystallographic description of VO_2 is given.

1.1 The Phases of Vanadium Dioxide

F. J. Morin first observed an insulator-metal transition in VO_2 as early as 1959 [2]. By heating above 340 K, an electrical conductivity increase of 2 orders of magnitude was reported. This first-order phase transition was associated with a change in crystallographic structure. In more stoichiometric samples, an increase in electrical conductivity of as much as 10^5 was observed [5].

Above 340 K (70 °C), VO_2 is observed to be in a metallic rutile crystal structure shown in Fig. 1–1. In the rutile system, vanadium atoms are arranged in a body-centered tetragonal Bravais lattice, with all vanadium atoms nearly perfectly octohedrally-coordinated.

While equally-spaced along the rutile c -axis (labeled \mathbf{c}_R -axis) in the rutile phase, the vanadium atoms dimerize when cooling below 340 K, effectively doubling the c lattice constant. The dimers tilt perpendicular to the \mathbf{c}_R -axis, alternating between two direction for adjacent vanadium chains. This lower-symmetry phase is the monoclinic M1 phase of VO_2 , presented in Fig. 1–1. All vanadium atoms are octohedrally-coordinated, as in the rutile structure. Monoclinic M1 VO_2 is a semiconductor with a narrow band gap of 0.6 eV [5].

Uniaxial stress or doping yields another phase of VO_2 with monoclinic character labeled M2 [1]. The monoclinic M2 VO_2 has a checkerboard-pattern of chains in which dimers are alternatively tilted and rotated [7]. This phase is also semiconducting.

Many physical properties of VO_2 change significantly during the monoclinic M1-rutile transition. Optical transmittance and electrical conductivity discontinuously jump by up to

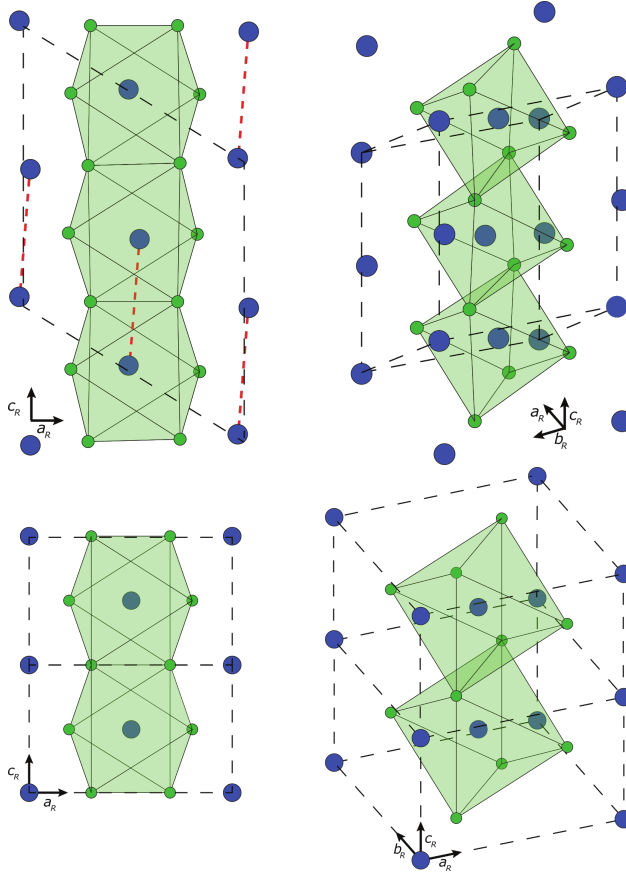


FIGURE 1–1: Crystallographic structure of VO₂. Oxygen atoms (green) form an octahedral cage (green overlay) around vanadium atoms (blue). **Top:** 3/2 unit cells of the insulating, low-temperature monoclinic M1 structure. **Bottom:** two unit cells of the metallic, high-temperature rutile structure. Figure adapted with permission from [6].

5 orders of magnitude, while magnetic susceptibility and specific heat also display discontinuities around the transition temperature [8].

1.2 Two Theoretical Models of the Insulator-Metal Transition of VO₂

This section presents two competing models for the insulator-metal transition of VO₂. The first model, proposed by Goodenough [9], argues for a crystal field picture of the lattice distortions giving rise to a band gap in the monoclinic M1 phase. The second model, put forward by Zylbersztejn and Mott [10], proposes that strong electronic correlations,

or the competition between localized and delocalized electrons, leads to an insulator-metal transition.

1.2.1 Peierls Distortions and The Goodenough Model

The first modelling study by Goodenough [9] considered changes in molecular orbitals and energies due to a structural phase transition, and attributed the insulator-metal transition to the Peierls-type lattice distortion of the low-temperature insulating phase.

The d-orbitals of vanadium are of particular interest to the insulator-metal transition because their energy levels are the lowest amongst orbitals of energy greater than the Fermi level [11]. Goodenough tells us that the five vanadium 3d-orbitals are split into two non-degenerate groups when the atom is placed in the VO₂ crystal potential, labeled t_{2g} (lower energy) and e_g (higher energy), as shown in Fig. 1–2. The two e_g orbitals d_{3z²-r²} and d_{xy} (also labeled d_{||}) are oriented towards the (octohedrally-coordinating) oxygen atoms, forming σ-type bonding and antibonding V3d-O2p orbitals. The t_{2g} orbital d_{x²-y²} is directed in the c_R-axis – y plane (in local coordinate system) while, d_{xz}, and d_{yz} are directed towards the faces of the unit cell.

The study presented by Goodenough describes that the band gap of monoclinic M1 VO₂ is caused by a lattice distortion, the V-V dimers. These dimers increase the d_{||} orbitals overlap, splitting the band into bonding (d_{||}) and antibonding (d_{||}^{*}) bands, the latter band sitting above the Fermi level. Additionally, the tilting of the V-V dimers away from alignment with the c_R-axis increases the energy of the π* band. The combination of these two effects opens a band gap [9]. A diagram of this band gap opening is shown on Fig. 1–3.

A Second Monoclinic Phase of VO₂

Experimental evidence later discredited the idea that lattice distortions alone were enough to explain the insulator band gap in monoclinic M1 VO₂. By chromium-doping

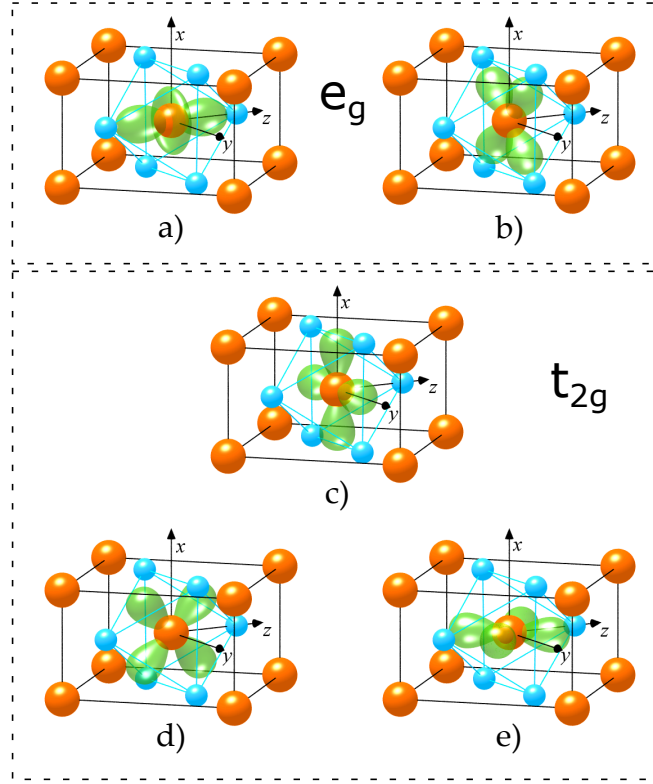


FIGURE 1–2: Graphical representation of the e_g and t_{2g} orbitals. e_g orbitals are labeled $d_{3z^2-r^2}$ (a) and $d_{xy} = d_{\parallel}$ (b). t_{2g} orbitals are labeled $d_{x^2-y^2}$ (c), d_{xz} (d) and d_{yz} (e). Figure adapted with permission from [7].

VO₂ polycrystalline samples, a second monoclinic phase, labeled M2, was observed [1]. The monoclinic M2 phase of VO₂ was later observed in samples under uniaxial stress along the [110]_R [12].

The monoclinic M2 phase is very similar to the monoclinic M1 structure but displays a checkerboard-like pattern, in which half of the vanadium chains along \mathbf{c}_R show dimerization, and half of the chains show tilting; this stands in contrast with the monoclinic M1 structure, in which all vanadium chains have tilted V-V dimers. While the Peierls-type lattice distortion disappears when transforming from monoclinic M1 to M2, the insulating behavior remains. This indicates that the dimerization along \mathbf{c}_R is not solely responsible for the opening of the insulating gap, as previously thought. The existence of the monoclinic M2 phase of VO₂

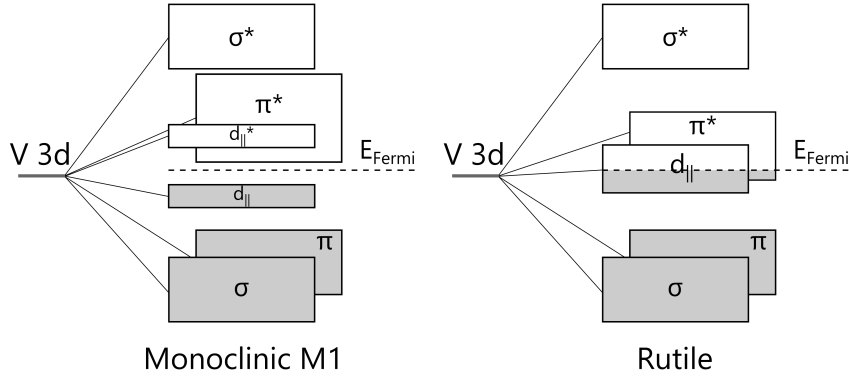


FIGURE 1–3: Diagram of the V 3d orbitals splitting between the monoclinic M1 and rutile structures of VO₂ [9].

also calls into question whether the structural phase transition induces an insulator-metal transition.

1.2.2 Strong Electronic Correlations and the Mott-Hubbard Model

The findings of Marezio et al. [1] prompted Zylbersztejn and Mott [10] to suggest an alternative mechanism explaining the insulating phases of VO₂. Their work took into account the competition between electronic localization and itineracy, minimizing the Coulomb potential energy due to double-occupancy repulsion via localization, and minimizing the electrons' kinetic energy through delocalization. A diagram of this competition is shown in Fig. 1–4.

This so-called Mott-Hubbard model is supported by experimental observations. Firstly, rutile VO₂ has low carrier mobility (on the order of 1 - 10 cm²/V/s), characteristic of strong electron-electron correlations. Secondly, photoexcitation using laser pulses induces an insulator-metal transition above a threshold fluence only, suggesting the existence of a threshold charge carrier density. Thirdly, this threshold fluence lowers as temperature increases [13].

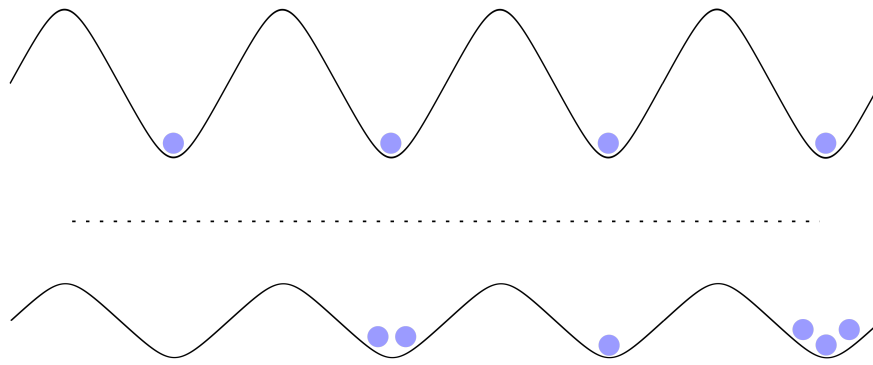


FIGURE 1–4: Diagram of the localized and delocalized electron states in a lattice. **Top:** localized electrons in a high lattice potential give rise to an insulating behaviour in VO_2 . **Bottom:** Low lattice potential favours delocalized electrons, which in turn increase conductivity but can result in multiple electron occupancy at each vanadium site. [10].

1.3 Simulations Studies

The phenomena of Peierls distortion and strong electronic correlations, presented in the previous section, need not operate in exclusion of each other. At first glance, nothing indicates that both mechanisms cannot cooperate to cause the insulator-metal transition. VO_2 is a structurally simple material. Its unit cell is small and has a relatively high symmetry in all phases. It is therefore a good playground for computational studies, of which some are briefly summarized in this section. The aim of such studies is to determine the relative contributions of electron-electron (Mott-Hubbard) and electron-lattice (Goodenough) interactions in the VO_2 insulator-metal transition.

Density-functional theory (DFT) involving the local density approximation (LDA) was used by Eyert [7] to investigate the phase transitions between rutile, monoclinic M1, and monoclinic M2 VO_2 . Surprisingly, this approach does not yield a band gap for the M1 and M2 phases unless the lattice distortions are exaggerated in such a way that the $d_{||}$ and π^* orbitals do not overlap.

In 2005, Biermann et al. [14] used dynamical mean-field theory (DMFT) combined with density field theory (DFT) to determine the role of electronic correlations. These simulations describe the M₁ phase to be insulating, with a band gap of 0.6 eV. It predicts that the insulating gap is due to the two d-orbital electrons of the vanadium dimers forming singlet states. The Biermann et al. results suggest that the role of the electronic correlations is to *renormalize* the split d_{||} band downwards in energy, which results in a band gap opening.

Weber et al. [15] applied DMFT + DFT on a structure composed of several VO₂ unit cells. In contrast with Biermann et al. [14], orbital occupations of vanadium and oxygen atoms were allowed to vary. An insulating state with crystallography of the M₁ phase was found, in which vanadium dimers were made of two d-orbital electrons. Weber et al. [15] goes on to suggest that VO₂ is really a Mott-type insulator, with the contribution from Peierls distortion being limited to enabling the Mott transition at on-site Coulomb repulsion energies expected in VO₂. Effectively, electron-lattice interactions are the main driving force behind the insulator-metal transition.

Note that Weber et al. [15] and Biermann et al. [14] are considering the insulator-metal transition of VO₂ to result from a combination of electron-lattice interactions (Goodenough model) and electron-electron interactions (Mott-Hubbard model).

The Biermann et al. [14] view of the insulator-metal transition is that of a Peierls-type insulator with assistance from a Mott instability, while the Weber et al. [15] view considered the phase transition to be mostly a Mott insulator enabled by a Peierls-type lattice distortion. These simulation studies present two likely scenarios that can be investigated by photoinducing (i.e. non-thermally inducing) the insulator-metal transition of VO₂.

1.4 Insulator-Metal Transition via Ultrafast Photoexcitation

An ultrafast laser pulse can also be used to drive the insulator-metal transition in VO₂, as first observed by Becker et al. [16]. Such ultrafast pulses drive electrons out of their ground

state, and effectively trigger the insulator-metal transition non-thermally on the femtosecond time-scale, effectively out-running other, slower effects.

This section aims at providing context for ultrafast photoinduction of the insulator-metal transition in VO₂. In Chapter 4, these concepts will be revisited through the work of Morrison et al. [17].

Using ultrafast time-resolved spectroscopy, Cavalleri et al. [18] reported a bottleneck of 75 fs for the photoinduced insulator-metal transition, roughly half of the V – V dimer vibration mode in VO₂. As a result, the author attributed the collapse of the band gap to structural motion, indicating that the structural transition is an essential precursor to the electronic transition. Interestingly, ultrafast terahertz spectroscopy have found an instrumentally-limited phase transition timescale of 60 fs, and that the threshold photoexcitation fluence required to trigger the insulator-metal transition decreases with initial sample temperature [19].

Baum et al. [20] used ultrafast electron diffraction in a reflection geometry and identified two timescales. They stated that this was likely a two-step structural rearrangement. The authors suggested an initial change with a first time-scale of 307 fs, associated with a lengthening of the vanadium dimers along their axis, and a second change with a time-scale of fs, associated with motion in the plane perpendicular to the V – V dimer axis, bringing the vanadium atoms to their final position in the rutile phase.

References

- [1] M. Marezio, D. B. McWhan, J. P. Remeika, and P. D. Dernier. Structural aspects of the metal-insulator transitions in Cr-doped VO₂. *Physical Review B*, 5(7):2541–2551, 1972.
- [2] F. J. Morin. Oxides which show a metal to insulator transition at the Néel temperature. *Physical Review Letters*, 3(1):34–36, 1959.
- [3] T. Driscoll, S. Palit, M. M. Qazilbash, M. Brehm, F. Keilmann, Byung-Gyu Chae, Sun-Jin Yun, Hyun-Tak Kim, S. Y. Cho, N. Marie Jokerst, D. R. Smith, and D. N. Basov. Dynamic tuning of an infrared hybrid-metamaterial resonance using vanadium dioxide. *Applied Physics Letters*, 93(2):024101, 2008.
- [4] Jeehoon Kim, Changhyun Ko, Alex Frenzel, Shriram Ramanathan, and Jennifer E. Hoffman. Nanoscale imaging and control of resistance switching in VO₂ at room temperature. *Applied Physics Letters*, 96(21):213106, 2010.
- [5] Larry A. Ladd and William Paul. Optical and transport properties of high quality crystals of V₂O₄ near the metallic transition temperature. *Solid State Communications*, 7(4):425–428, feb 1969.
- [6] Vance R. Morrison. *Structural dynamics of the metal-insulator transition in VO₂: an ultrafast electron diffraction study with radio-frequency compressed electron pulses*. PhD thesis, McGill University, 2014.

- [7] Volker Eyert. The metal-insulator transitions of VO_2 : A band-theoretical approach. *Ann. Phys. (Leipzig)*, 11:650–702, 2002.
- [8] C. N. Berglund and H. J. Guggenheim. Electronic Properties of VO_2 near the Semiconductor-Metal Transition. *Physical Review*, 185(3):1022–1033, sep 1969.
- [9] John B. Goodenough. The two components of the crystallographic transition in VO_2 . *Journal of Solid State Chemistry*, 3(4):490–500, 1971.
- [10] A. Zylbersztein and N.F. Mott. Metal-insulator transition in vanadium dioxide. *Physical Review B*, 11(11):4383–4395, 1975.
- [11] P. A. Cox. *Transition Metal Oxides*. Oxford University Press, Oxford, 1992.
- [12] J. P. Pouget, H. Launois, J. P. D’Haenens, P. Merenda, and T. M. Rice. Electron Localization Induced by Uniaxial Stress in Pure VO_2 . *Physical Review Letters*, 35(13):873–875, 1975.
- [13] Luisa Whittaker, Christopher J. Patridge, and Sarbajit Banerjee. Microscopic and nanoscale perspective of the metal-insulator phase transitions of VO_2 : some new twists to an old tale. *Journal of Physical Chemistry Letters*, 2(7):745–758, 2011.
- [14] S. Biermann, A. Poteryaev, A. I. Lichtenstein, and A. Georges. Dynamical singlets and correlation-assisted peierls transition in VO_2 . *Physical Review Letters*, 94(2), 2005.
- [15] Cedric Weber, David D. O’Regan, Nicholas D. M. Hine, Mike C. Payne, Gabriel Kotliar, and Peter B. Littlewood. Vanadium dioxide: A Peierls-Mott Insulator Stable Against Disorder. *Physical Review Letters*, 108(25):1–5, 2012.
- [16] Michael F. Becker, A. Bruce Buckman, Rodger M. Walser, Thierry Lepine, Patrick Georges, and Alain Brun. Femtosecond laser excitation of the semiconductor-metal phase transition in VO_2 . *Applied Physics Letters*, 65(12):1507, 1994.
- [17] Vance R. Morrison, Robert P. Chatelain, Kunal L Tiwari, Ali Hendaoui, Andrew Bruhacs, Mohamed Chaker, and Bradley John Siwick. A photoinduced metallic phase of

- monoclinic VO₂ revealed by ultrafast electron diffraction. *Science*, 341(6208):19, 2014.
- [18] A. Cavalleri, H.H.W. Chong, R.W. Schoenlein, J.C. Kieffer, and Th. Dekorsy. Structural bottleneck in the photo-induced insulator to-metal transition in VO₂. *Physical Review B*, 70, 2004.
- [19] C Kübler, H Ehrke, R Huber, R Lopez, A Halabica, R F Haglund, and A Leitenstorfer. Coherent structural dynamics and electronic correlations during an ultrafast insulator-to-metal phase transition in VO₂. *Physical review letters*, 99(11):116401, sep 2007.
- [20] Peter Baum, Ding-Shyue Yang, and Ahmed H. Zewail. 4D Visualization of Transitional Structures in Phase Transformations by Electron Diffraction. *Science*, 318(5851):788–792, 2007.

CHAPTER 2

Electron Diffraction Formalism

This section details how electron scattering on crystals is used to investigate the structural and electronic properties of samples. The electron diffraction theory is derived from [1].

The idea behind scattering potential maps, the main subject of this work, is also introduced below. While the theory behind representing crystal potential can be succinctly explained, Chapter 4 is dedicated to the computation of such maps using experimental data.

2.1 Scattering

Consider a source of electrons. If the source of electrons is far enough from the scattering potential, we can consider the incoming electrons as a plane wave (this is the far-field approximation):

$$\Psi_I(\mathbf{r}) = e^{i(\mathbf{k}_I \cdot \mathbf{r} - \omega t)} \quad (2.1)$$

where \mathbf{k}_I is the wavevector of incident electrons, and \mathbf{r} is the source-scatterer vector. Scatterers interacting with an incident electron plane wave will scatter into a spherical wave of the following form:

$$\Psi_S = f(\mathbf{k}_I, \mathbf{k}_S) \frac{e^{i|\mathbf{k}_S||\mathbf{r}'|} e^{-i\omega t}}{|\mathbf{r}'|} \quad (2.2)$$

where \mathbf{k}_S is the wavevector of scattered electrons, and \mathbf{r}' is the scatterer-observer vector. The scalar function $f(\mathbf{k}_I, \mathbf{k}_S)$ is called the scattering amplitude, and depends on the orientation of the incident and scattered wavevectors in general. If we assume that the total field in the scatterer is a small perturbation of the incident field, we can assume that there is no loss in momentum ($|\mathbf{k}_I| = |\mathbf{k}_S|$). In this case, the scattering amplitude of Eq. 2.2 takes the form:

$$f(\mathbf{k}_I, \mathbf{k}_S) = -\frac{m}{2\pi\hbar^2} \int V(\mathbf{r}) e^{i(\mathbf{k}_S - \mathbf{k}_I) \cdot \mathbf{r}} d^3 \mathbf{r} \quad (2.3)$$

where $V(\mathbf{r})$ is the scattering potential for electrons, the electrostatic potential. Note that Eq. 2.3 shows that the scattering amplitude is proportional to the Fourier transform of the scattering potential.

Experimentally, detectors probe the intensity of the scattered wave of Eq. 2.2, which is proportional to the amplitude of the scattering amplitude of Eq. 2.3. Measurements are made easier by probing systems in which the scattering potential $V(\mathbf{r})$ is periodic. One type of such system, and the main system studied in this work, is a crystal.

2.2 Scattering in Crystals: Diffraction

Crystals are periodic arrangements of atom. The smallest non-spatially-periodic set of atoms is called the unit cell. A crystal possesses a discrete translational symmetry equal to the dimensions of the unit cell.

The unit cell can be described by three linearly independent (but generally non-orthogonal) lattice vectors \mathbf{a}_i . If $\mathbf{r} = \sum n_i \mathbf{a}_i$ is on a lattice point ($n_i \in \mathbb{Z}$), then constructive interference of scatterers with wavevector \mathbf{k}_S (be it X-rays or electrons) occurs whenever the *von Laue* condition is satisfied:

$$e^{i\mathbf{r} \cdot (\mathbf{k}_S - \mathbf{k}_I)} = 1 \quad (2.4)$$

which can be rewritten as $\mathbf{r} \cdot \Delta \mathbf{k} = 2\pi m$ for some integer m . The set of wavevectors $\{\mathbf{G} = \Delta \mathbf{k}\}$ satisfying Eq. 2.4 are known as reciprocal lattice points. Similarly to the real-space lattice,

we can define reciprocal lattice vectors denoted \mathbf{b}_j spanning the reciprocal space. Formally, this reciprocal basis is defined as follows:

$$\mathbf{a}_i \cdot \mathbf{b}_j = 2\pi\delta_{ij} \quad (2.5)$$

Then, any allowed wavevector can be written as $\mathbf{G} = h\mathbf{b}_1 + k\mathbf{b}_2 + l\mathbf{b}_3$ for $h, k, l \in \mathbb{Z}$. The integers h , k , and l are known as the Miller indices.

From equation Eq. 2.5, the reciprocal lattice vectors can be computed:

$$\mathbf{b}_i = 2\pi \frac{\mathbf{a}_j \times \mathbf{a}_k}{\mathbf{a}_i \cdot (\mathbf{a}_j \times \mathbf{a}_k)} \quad (2.6)$$

for cyclic permutation of $(1, 2, 3)$.

2.2.1 Structure Factors

Inserting the periodic potential of a crystal lattice in Eq. 2.2 reveals the amplitude for the scattered wave, called the structure factor:

$$S(\mathbf{G}) = \sum_j f_j(\mathbf{G}) e^{-i(\mathbf{G} \cdot \mathbf{r}_j)} \quad (2.7)$$

where $f_j(\mathbf{G})$ is an individual atom's scattering amplitude from Eq. 2.3 and the sum is over all atoms in the unit cell. Measurements probe the scattered wave intensity, and therefore diffracted intensities are proportional to $|S(\mathbf{G})|^2$. Since structure factors are complex in general, diffraction alone does not yield enough information to completely solve the structure factors, as the complex phase is not measured.

2.2.2 Visualizing Diffraction Conditions with the Ewald Sphere

To diffract elastically, wavevectors must satisfy two conditions:

- Momentum conservation ($|\mathbf{k}_I| = |\mathbf{k}_S|$). This leads to the simple form of Eq. 2.3;
- Constructive interference, i.e. the von Laue condition from Eq. 2.4.

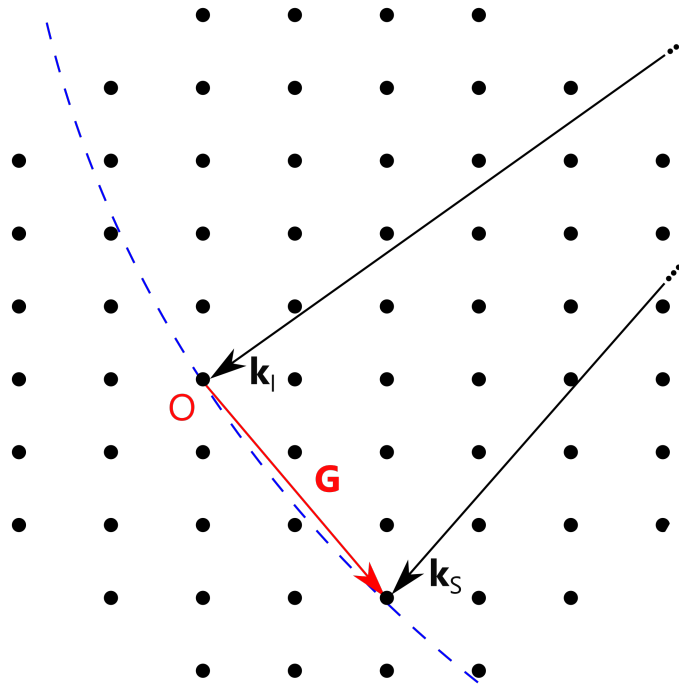


FIGURE 2–1: Elastic scattering experiments measure the diffracted intensity at wavevectors \mathbf{G} (red) where the Ewald sphere (blue, dashed) coincides with the reciprocal lattice.

These two conditions are geometrically represented (for a hypothetical two-dimensional crystal) in Fig. 2–1. Elastic diffraction occurs wherever the Ewald sphere, made of momentum-conserving wavevectors, and the reciprocal lattice, describing momentum-conserving scattering vectors, coincide.

Assuming monochromatic scattering and an infinite crystal, the Ewald sphere's shell is infinitely thin and reciprocal lattice sites are infinitely small, so that diffraction should occur only for $|\mathbf{G}| = 0$. However, in experiments, a spread in scatterer momentum/energy thickens the Ewald sphere, while crystal size effects spreads the reciprocal lattice points over finite volume in reciprocal space. In order to sample more scattering vectors, the scatterer (e.g.

crystal sample) is rotated, so that the Ewald sphere intersects different reciprocal lattice points

Of note is that the radius of the Ewald sphere is proportional to the scattering wavevector amplitude $\mathbf{k}_I \propto \frac{1}{\lambda}$. Since electrons have a much smaller wavelength than x-rays, the Ewald sphere for electron diffraction is almost flat close to $|\mathbf{G}| = 0$. Therefore, the electron Ewald sphere will intersect many more scattering vectors \mathbf{G} at a given scatterer orientation relative to the crystal.

2.3 Scattering Potential Maps

In order to visualize time-resolved scattering potential from diffraction data, we apply the inverse Fourier transform to the function composition of Eq. 2.2 and Eq. 2.3. Taking the real part yields:

$$\phi(\mathbf{r}, t) = \sum_{\{\mathbf{G}\}} |S(\mathbf{G}, t)| e^{i\chi(\mathbf{G}, t)} \cos(\mathbf{G} \cdot \mathbf{r}) \quad (2.8)$$

where $\chi(\mathbf{G}, t)$ is the phase of the (generally complex) structure factor $S(\mathbf{G}, t)$, $|S(\mathbf{G}, t)| = \sqrt{I(\mathbf{G}, t)}$, and $\phi(\mathbf{r}, t)$ is the scattering potential in real space [2]. In the case of electron diffraction, the scattering potential is the total electrostatic potential while in x-ray diffraction experiments, photons are scattered by the electron charge density.

Determining the phase $\chi(\mathbf{G}, t)$ *ab initio* is a difficult problem, and it is circumvented by studying materials with known equilibrium structures, such as VO₂. In the case of vanadium dioxide, the unit cell is centrosymmetric; then $\chi(\mathbf{G}, t) \in \{0, \pi\}$. This work assumes that the phase will not change during dynamics (that is, phases $\chi(\mathbf{G}, t)$ will not flip between 0 and π), which is an acceptable assumption provided that the heavy atoms don't move too much during photoexcitation [3].

2.4 The Patterson Function

The Patterson function is introduced because it can be calculated in two different ways: directly from diffraction intensities, and through scattering potential maps. It is therefore a good test for the validity of the scattering potential mapping approach, and will be used in Chapter 4.

The Patterson function is defined as the autocorrelation in real-space of the crystal scattering potential $\phi(\mathbf{r}, t)$:

$$P(\mathbf{r}) = \int_V \phi(\mathbf{u})\phi(\mathbf{u} + \mathbf{r})d\mathbf{u} \quad (2.9)$$

The vectors between the origin and local extrema of the Patterson reveals the atomic distances $\mathbf{a}_i - \mathbf{a}_j$, weighed proportionally by their respective atomic form factors $f_i f_j$ [2].

To compute the Patterson function from diffraction data, the diffracted intensity is normalized to produce the *reduced intensity*:

$$\mathcal{I}(\mathbf{G}) = \frac{I(\mathbf{G})}{\sum_j |f_j(\mathbf{G})|^2} \quad (2.10)$$

where the sum is over all atoms j in the unit cell. This normalization counteracts the decrease in diffracted intensities with increasing $|\mathbf{G}|$. Then, the Patterson function is given by:

$$P(\mathbf{r}) = \frac{1}{V^2} \sum_{\{\mathbf{G}\}} \mathcal{I}(\mathbf{G}) e^{\mathbf{G} \cdot \mathbf{r}} \quad (2.11)$$

The radial average of the Patterson function $P(\mathbf{r})$, is called the radial pair-distribution function and denoted $G(r)$. It is an essential tool in powder diffraction analysis in order to link diffraction intensities to real-space length scales [2, 4].

2.5 Addendum: Sensitivity to Atomic Form Factor Changes

Transmission electron diffraction maps the total electrostatic crystal potential of a sample. This is the primary distinction between electron and X-ray diffraction; X-rays interact

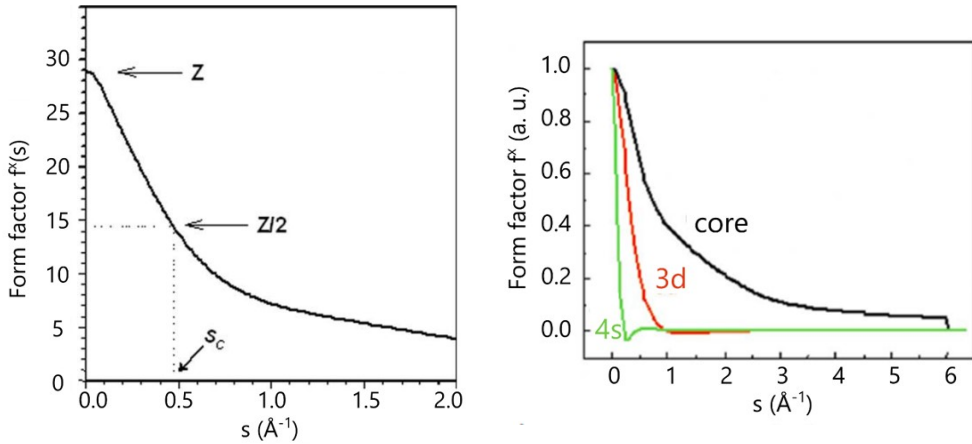


FIGURE 2–2: **Left:** x-ray form factor of Cu. Electron diffraction is more sensitive to valence charge distribution changes than X-ray diffraction in the regions where $f^x(s) > Z/2$ ($s_c = 0.47 \text{ \AA}^{-1}$). **Right:** contribution of individual electron orbital to the X-ray form factor of Cu [5].

with the electron density while electrons interact with the total charge density. Electron diffraction provides a sensitive probe of both lattice and valence electronic structure.

The atomic form factors for electron scattering are very sensitive to the occupancy of the valence shells. This can be seen by relating the atomic form factors for X-ray (f^x) and electron (f^{e^-}) using the Mott-Bethe formula:

$$f^{e^-}(|\mathbf{G}|) \propto \frac{1}{|\mathbf{G}|^2} [Z - f^x(|\mathbf{G}|)] \quad (2.12)$$

where Z is the atomic number [4, Appx. C]. Eq. 2.12 shows that electron structure factors of low-index (i.e. small $|\mathbf{G}|$) are very sensitive to valence charge density distribution [5].

References

- [1] B. Fultz and J. M. Howe. *Transmission Electron Microscopy and Diffractometry of Materials*. Springer, Berlin, second edi edition, 2002.
- [2] W.I.F. David, K. Shanklannd, L.B. McCusker, and Ch. Baerlocher. *Structure determination from powder diffraction data*. Oxford University Press, New York, 2002.
- [3] Thomas Elsaesser and Michael Woerner. Photoinduced structural dynamics of polar solids studied by femtosecond X-ray diffraction. *Acta Crystallographica Section A: Foundations of Crystallography*, 66:168–178, 2010.
- [4] Earl J. Kirkland. *Advanced Computing in Electron Microscopy*. Springer, New York, second edition, 2010.
- [5] Jin Cheng Zheng, Yimei Zhu, Lijun Wu, and James W. Davenport. On the sensitivity of electron and X-ray scattering factors to valence charge distributions. *Journal of Applied Crystallography*, 38(4):648–656, 2005.

CHAPTER 3

Data Acquisition and Processing

This chapter is devoted to the explanation of the data processing pipeline, from acquisition to physically-relevant diffraction intensities. The main instrument responsible for data acquisition is an ultrafast electron diffractometer, described below in the first section. A sketch of the data acquisition pipeline is subsequently presented.

The chapter ends with a description of two features that affect the diffraction intensities extraction: the inelastic scattering background as well as polycrystalline textures. These effects are especially important to the analysis of Chapter 4 due to the scattering potential maps' sensitivity to diffraction intensities.

3.1 Experimental Setup

3.1.1 Overview

The ultrafast electron diffractometer is best explained with the analogy of a photography setup. In order to capture fast movement, a camera must expose the film for a very short time using a fast shutter. This fast shutter comes with a trade-off of brightness: low exposition photographs will be dark.

The ultrafast electron diffractometer faces similar challenges. To resolve fast dynamics in a sample, scattered electrons must move as a very tight bunch, equivalent to an ultrafast

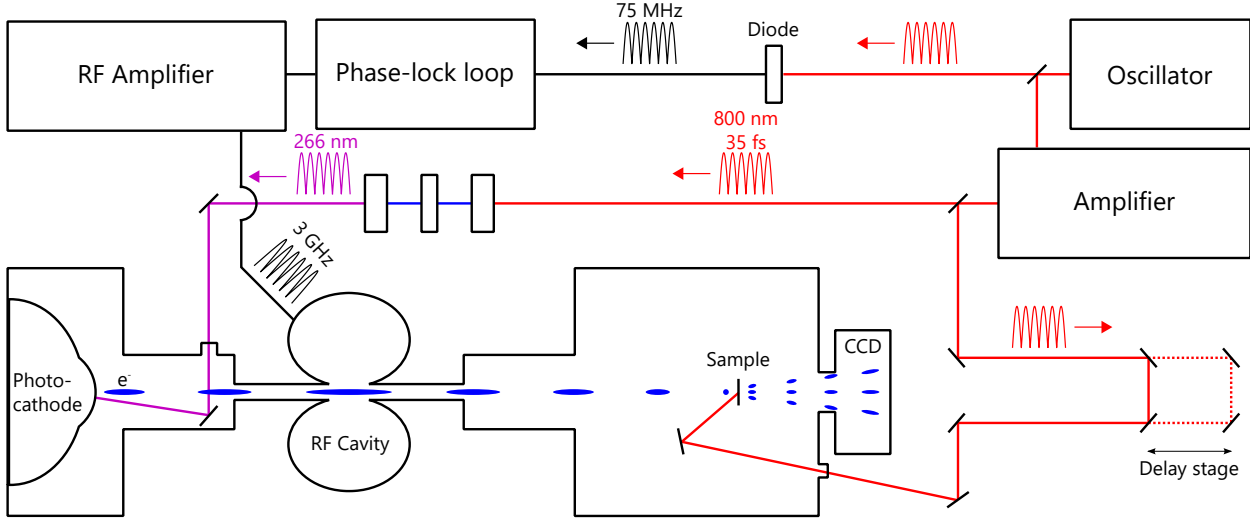


FIGURE 3–1: Diagram of the ultrafast electron diffractometer. An oscillator drives both a laser amplifier and a phase-lock loop. The laser beam is split between a pump and a probe, while the phase-lock loop synchronizes an amplified RF cavity to the pump and probe beams. The RF cavity acts as a temporal lens to focus the probe electron beam onto the sample.

shutter. These electron bunches are made from 1×10^6 - 10×10^6 electrons (high brightness) to lower experiments time. However, dense electron bunches tend to stretch in space due to the Coulomb repulsion between charges [1]. The solution employed in the Siwick research group is a essentially a focusing 'lens', a radio-frequency (RF) cavity designed so that the bunches are focused at the sample [2]. This RF-cavity is synchronized to the laser via a phase-lock loop.

A simplified diagram of the ultrafast electron diffractometer is presented in Fig. 3–1.

3.1.2 Laser System

The laser system and synchronization scheme is built around a titanium sapphire laser oscillator (Newport Tsunami) producing 35 fs pulses at a repetition rate of 75 MHz. Each oscillator pulse carries about 5 nJ of energy. The oscillator pulses are split by a 95/5 beam splitter.

5% of the oscillator power is used as a reference signal for a phase-lock loop that synchronizes the RF compression cavity to the electron bunch generation. See Section 3.1.4 for more details.

The other 95% of the oscillator power is used to seed a laser amplifier (Spitfire Pro). The laser amplifier outputs 35 fs pulses at a repetition rate of 1 kHz with center wavelength of 800 nm. Each amplified laser pulse carries 3 mJ of energy, with total power being 3 W. The amplified laser pulses are split into a pump beam and a probe beam.

The pump beam pulses go through a delay stage (lower right corner of Fig. 3-1) that can move about 20 cm in steps of 1 μm . This corresponds to a maximum pump-probe delay of 1.3 ns, adjustable in steps of 5 fs. The pump laser power can be attenuated by using a waveplate-polarizer combination. The pump beam is then steered onto the sample. The pump beam spot size on the sample is made adjustable by moving a lens outside the sample chamber.

The probe beam, initially with a center wavelength of 800 nm, is frequency-tripled to 266 nm. This is done by having the probe laser beam go through a beta-phase barium borate (BBO) crystal, converting a portion of the 800 nm light into 400 nm light using type I second-harmonic generation (SHG). The pulses then go through a birefringent calcite crystal to correct for the difference in group velocities between 800 nm light and 400 nm light. Finally, the 800 nm light and 400 nm light pass through another BBO crystal. This second BBO crystal is used in a type II sum frequency generation scheme, which creates 266 nm light polarized orthogonal to the original 800 nm light. The 266 nm ultra-violet (UV) light is separated from the other wavelengths by making use of a prism compressor. The UV light takes a different path than other wavelengths, and therefore can be spatially isolated. The UV pulses are then steered into the electron gun.

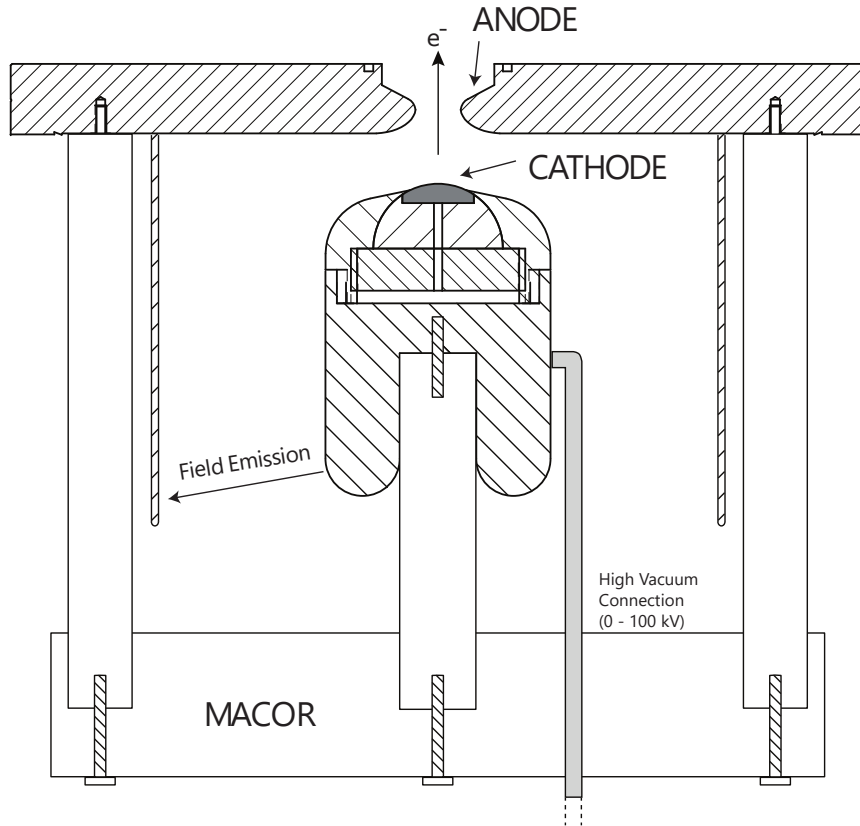


FIGURE 3–2: High voltage electron accelerator design rated up to 100 kV. Macor parts (white) support the cathode structure, and stainless steel (hatched) is used to shield Macor from emitted electrons. Figure adapted with permission from [3]

3.1.3 Electron Beam Generation

The electron bunches are generated by femtosecond laser pulses with a wavelength of 266 nm hitting a copper photocathode in an electron accelerator chamber (also called electron gun). Electrons are then accelerated inside the gun by strong DC fields. The typical potential difference between the photocathode piece and the anode disc is around 90 kV. A cross-section of the electron gun is presented on Fig. 3–2.

In order to avoid high voltage breakdown (incapacitating the electron accelerator), the chamber is kept at a pressure of at 10^{-6} torr by an Edwards turbomolecular pump.

3.1.4 Radio-frequency Compression of Electron Bunches

In order to achieve femtosecond time-resolution on diffraction experiment, electron bunches must be kept as short as possible: this is the equivalent of very short exposure in photography. However, due to the Coulomb repulsion between electrons, short bunches produced from high-brightness sources will expand as much as a few tens of picoseconds in resolution [1]. This *space-charge effect* introduces a trade-off between a high signal-to-noise ratio (electron beam current) and time-resolution (short electron bunches, equivalent to high shutter speed).

The trade-off between brightness and time-resolution can be overcome by employing a radio-frequency compression cavity (RF cavity) that acts as a temporal lens on the probe electron beam [2]. It applies a time-varying transverse electric-field synchronized to the probe laser beam that speeds up slow electrons at the back of the bunch, and slows down electron at the front of the bunch. This action effectively rotates the electrons in phase-space so that at the sample, all electrons are at the same transverse position with the same transverse momentum. The RF cavity drawings are presented on Fig. 3–3

3.1.5 Sample Chamber

The sample chamber is a stainless steel cube of side length 20 cm. It contains a three-axis translation stage supporting a sample holder. The stage is wired to a controller outside the chamber, enabling remote control. A second Edwards turbomolecular pump is used to pump down to 10^{-6} torr in minutes.

The sample chamber also has an angled window, through which the pump laser pulses pass. An alignment mirror is kept in the sample chamber, and its orientation is tweaked after a new sample is installed into the chamber.

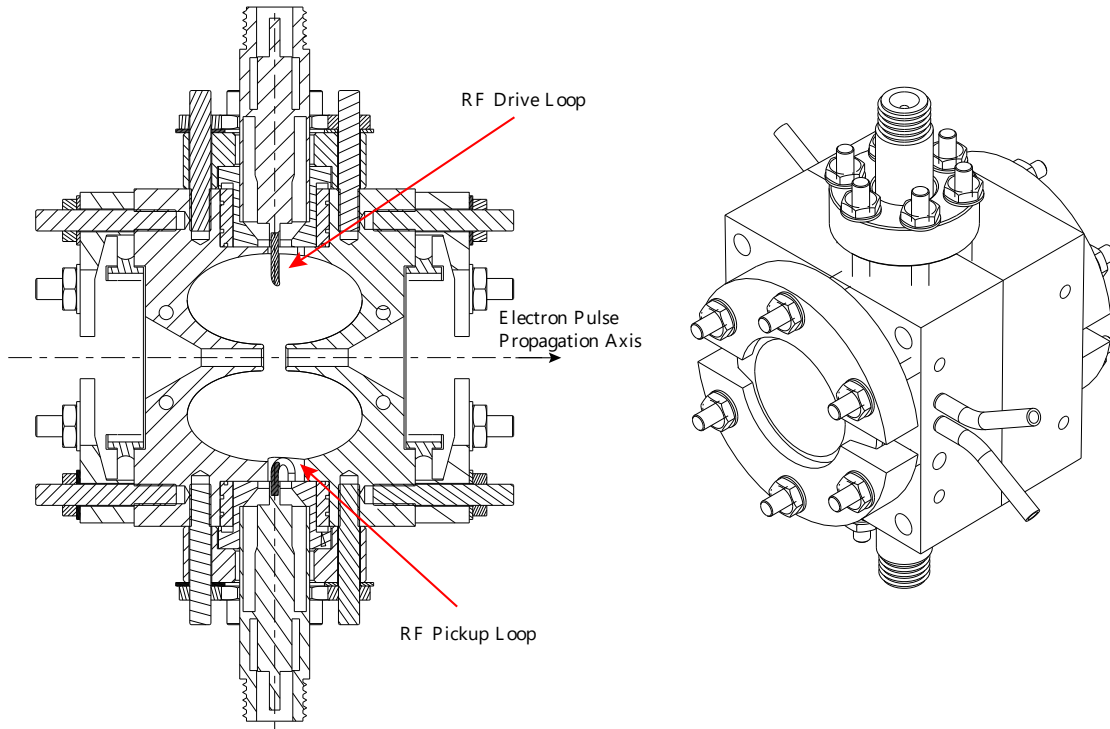


FIGURE 3–3: Schematic of the radio-frequency electron compression cavity presented by Van Oudheusden et al. [2]. Figure adapted with permission from [3]

3.1.6 Detection

Diffraction patterns are acquired by a Gatan UltraScan 1000 CCD camera. The CCD chip has dimensions $28.7 \text{ mm} \times 28.7 \text{ mm}$, and a resolution of $2048 \times 2048 \text{ px}^2$ (pixel width $\sim 14 \mu\text{m}$). A fibre-optically coupled phosphor film is installed over the CCD chip to generate light from impacting electrons. A 300 nm-thick film of aluminum was deposited on top of the phosphor to reflect any pump laser light from illuminating the CCD chip.

Reducing thermal noise is done by cooling the camera with a thermo-electric cooling module. Moreover, the CCD chip can be retracted into a vacuum chamber inside the camera, preventing condensation from forming when the sample chamber is opened. When the camera is cooled to $-25 \text{ deg } ^\circ\text{C}$, total electronic noise amounts to $\pm 2 \text{ counts/pixel}$.

3.2 Data Acquisition and Processing

This section will go through the process of acquiring time-resolved data and processing it for further analysis.

3.2.1 Acquisition Procedure

In order to acquire a diffraction dataset with ultrafast dynamics, a pump-probe scheme is employed. As shown in Fig. 3–1, the ultrafast laser pulses are split into a pump line and a probe line. By varying the path length of the pump line, the electron beam will illuminate a sample at an arbitrary time-delay before or after photoexcitation.

To acquire a time-resolved dataset implies diffracting from the sample for an array of time-delays. A typical time-delay array would be would go from -10 ps to 50 ps in variable steps (between 100 fs and 1 ps). A single diffraction picture per time-delay does not usually yield enough signal; therefore, this time-delay ‘scanning’ is repeated between 10 and 25 times, depending on the exposure time of the diffraction pictures.

3.2.2 Image Processing

After diffraction patterns have been acquired, the first step is to average all pictures at the same pump-probe delay. This reduces dataset size from hundreds of GiB to less than 1 GiB. A pump-laser-off background is then subtracted from these meta-images. To remove the influence of the sample substrate, diffraction patterns from an empty substrate is also averaged and subtracted from the meta-images.

For polycrystalline samples (such as the VO_2 samples used for this work), diffraction images consist of concentric Debye-Scherrer rings (see Fig. 3–4). Circles are fit to the images, in order to find the diffraction center, and the images are radially-averaged to yield radial diffraction patterns. Pixels located under the beamblock mask (red rectangle in Fig. 3–4) are not used in the average calculation.

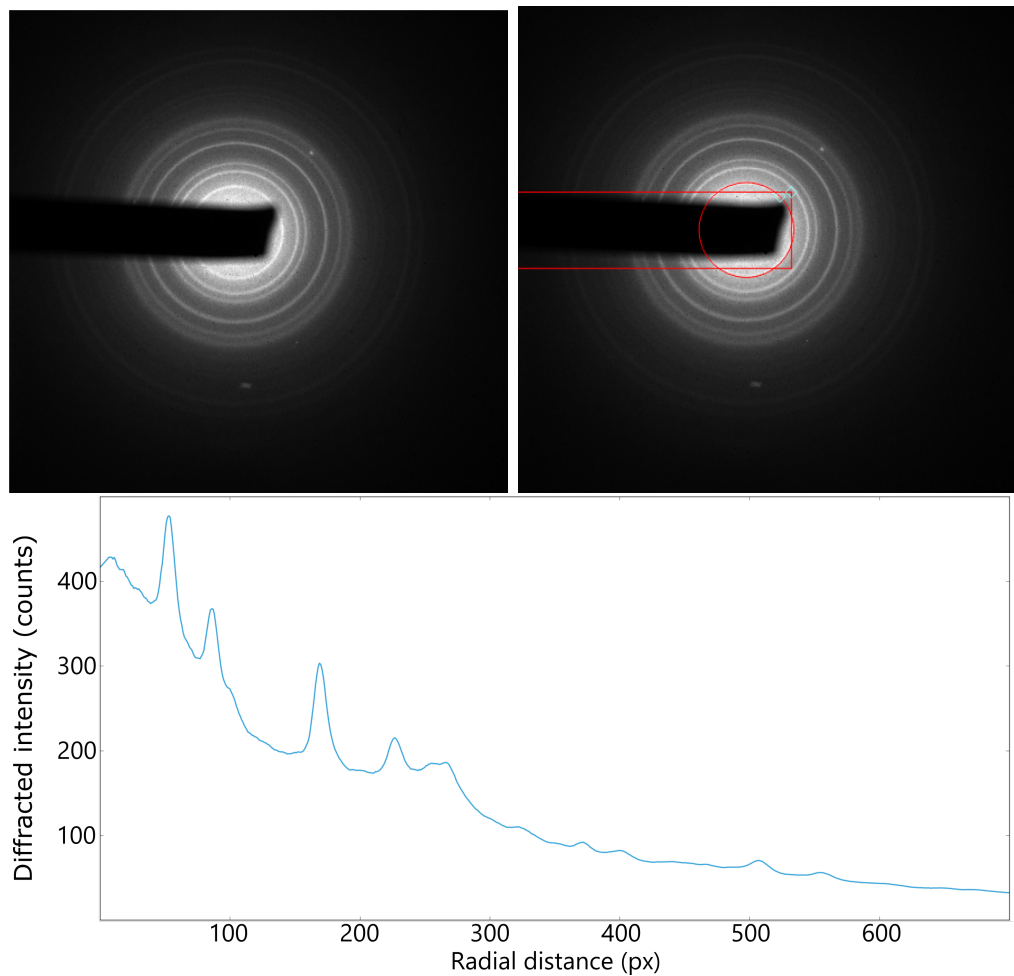


FIGURE 3–4: **Top left:** raw diffraction image of a polycrystalline sample of VO₂ before photoexcitation. **Top right:** Raw diffraction image of polycrystalline sample of VO₂, with Debye-Scherrer rings fit, as well as beamblock mask. **Bottom:** radial average, showing a low-frequency background, as well as elastic scattering peaks.

3.3 Polycrystalline Texture

In thin polycrystalline samples, crystallite orientations often roughly align with a *preferred orientation*. Depending on the crystal structure and material properties, crystallites can form rods or platelets which are too long to align perpendicularly to the sample surface [4].

The existence of preferred orientation(s) in a sample will affect the distribution of intensities, and thus can introduce artifacts in analyses that depend on accurate diffraction intensities. In the most extreme case, a sample consisting of a single crystallite, a single crystal, will not display Debye-Scherrer diffraction rings. Certain preferred orientations will yield radially assymmetric Debye-Scherrer rings, while others will have entire rings disappear.

This section is qualitative. The processing of texture data is computationally very intensive. The techniques presented herein are exploratory in nature. Further work is required before diffraction data can be corrected for polycrystalline texture.

3.3.1 Orientation Data

The microtexture (i.e. spacially-dependent texture at small scale) for the VO₂ sample used in this work is presented in Fig. 3–5. The microtexture was determined by electron back-scatter diffraction at McGill. The data set includes a list of crystallite areas, location in the sample, as well as the three Euler angles (Bunge convention) determining the crystallite normal direction. The crystallite normal directions were plotted on a hemisphere, showing the existence of two related preferred-orientations, shown on Fig. 3–6. While the information is only qualitative at this point, it stresses the fact that the polycrystalline samples used in [5] are far from ideal.

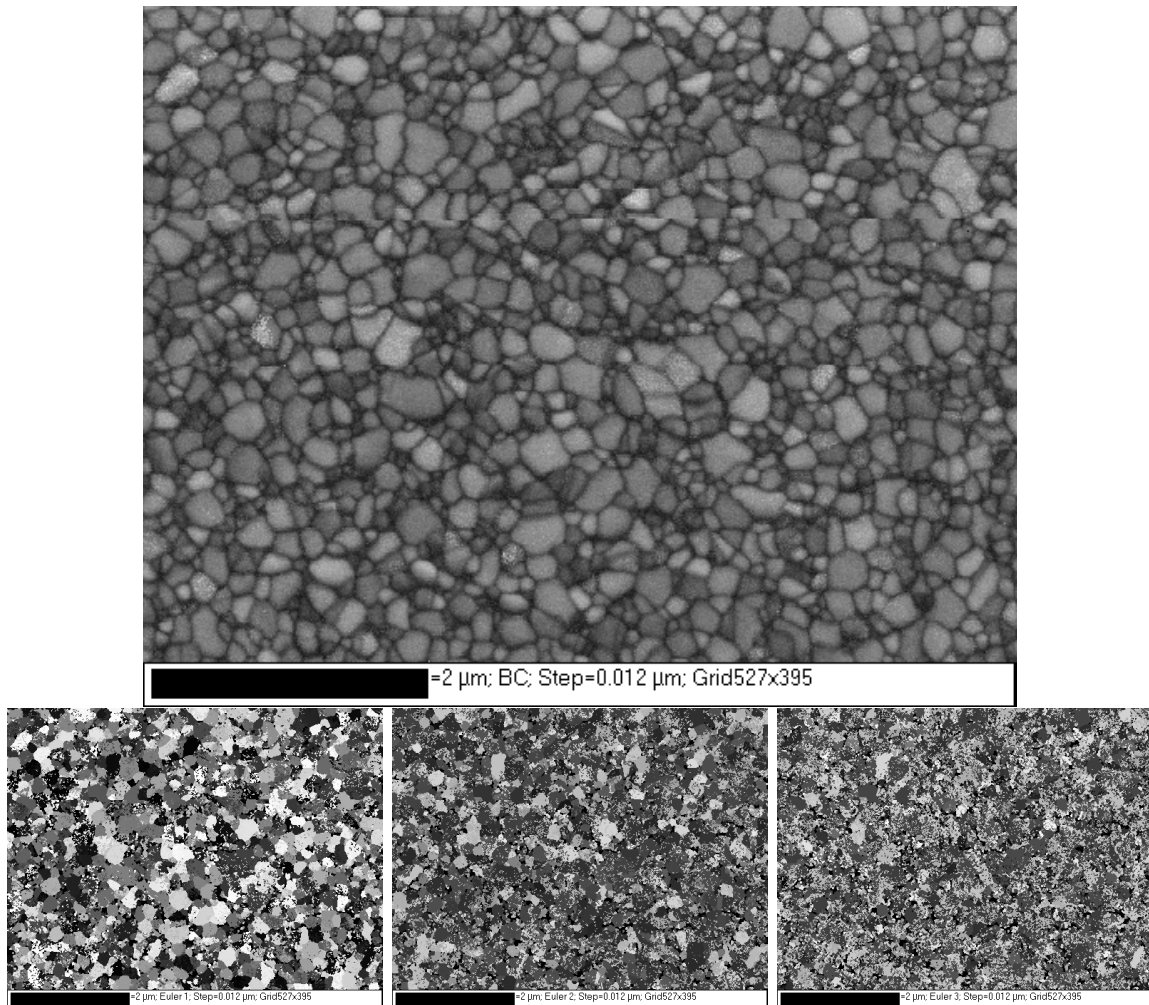


FIGURE 3–5: Texture data taken from the VO_2 sample used in this work. **Top:** SEM image of the sample surface, showing crystallite sizes. **Bottom:** spacial distribution of crystallite normals, computed from EBSD data, separated into Euler angles E1, E2, and E3 (left to right).

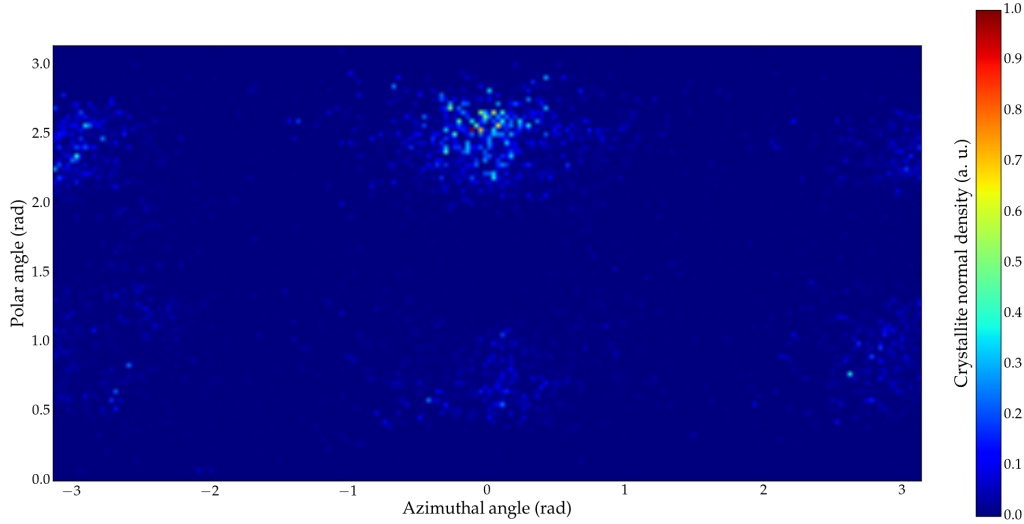


FIGURE 3–6: Distribution of crystallite normal directions (pole [100]) of a VO₂ sample using angular data from Fig. 3–5 uncorrected for crystallite area. The distribution shows the presence of preferred orientations.

3.3.2 Texture Correction via Pole Density

The pole density represents the fraction of poles (i.e. scattering vectors \mathbf{G}) on the surface of the unit sphere. It is represented by:

$$W(\theta, \phi) = \frac{dV}{V} \frac{4\pi}{d\Omega} \quad (3.1)$$

where θ and ϕ are the polar and azimuthal angles, and $\frac{dV}{V}$ is the fraction of crystallite volume within the solid angle defined by $\theta + d\theta$ and $\phi + d\phi$ [6]. In the ideal case of perfectly random orientation, $W_{ide}(\theta, \phi) \equiv 1$.

To compute the pole density, the set of scattering vectors \mathbf{G} is determined for a crystallite orientation with normal parallel to \hat{z} . An orientation matrix is associated with each crystallite orientation, and the set of scattering vectors for each crystallite is rotated according to the crystallite's orientation matrix. The total pole density is a weighted sum (with weights as crystallite areas, as volume data was unavailable) of individual crystallite's pole density. The

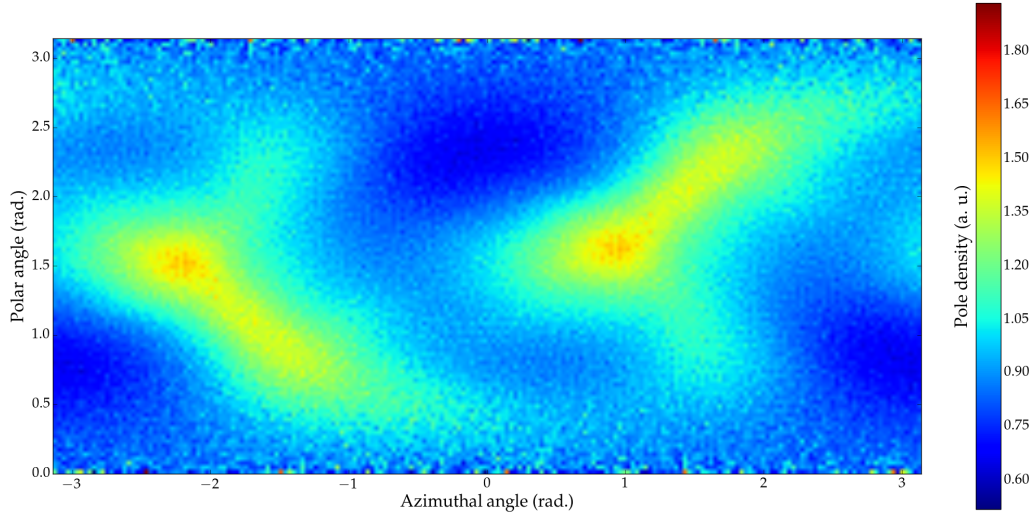


FIGURE 3–7: Pole density for the VO₂ sample used in this work. A pole density higher than unity signifies an over-represented scattering vector orientation.

results are plotted on Fig. 3–7, which shows that the two preferred-orientations are opposite orientations.

Once the pole density $W(\theta, \phi)$ is known, and from the knowledge of the spherical coordinates of each scattering vector, a pole density as a function of scattering vector $W(\mathbf{G})$ is calculated. Then, the diffracted intensity is corrected:

$$I(\mathbf{G}, t) \longrightarrow \frac{I(\mathbf{G}, t)}{W(\mathbf{G})} \quad (3.2)$$

3.4 Baseline Determination Using the Discrete Wavelet Transform

Powder diffraction patterns calculated from raw images (Fig. 3–4) can be affected by various effects contributing to an overall baseline. This baseline is composed of intensity offsets (from varying electron beam brightness), inelastic scattering from the sample, as well as scattering from the substrate.

Generally, this diffraction baseline is fit by a biexponential or bilorentzian function [5, 7, 8]. Elastic peaks (and therefore, background regions between the peaks) are hard to identify without prior knowledge of a structure, and thus curve fitting routines are highly dependent on the experimenter's estimations. This is in addition to the unstable nature of fitting to models with a numerous degrees of freedom.

The baseline of a powder diffraction pattern is usually low-frequency in reciprocal space. On the other hand, the elastic scattering signal that we wish to isolate is composed of a broad band of frequencies, generally overlapping with the baseline spectrum. Fourier techniques and digital filtering are therefore inadequate [9].

Wavelet transforms are widely applied to remove unwanted background, correct for wandering baselines , and peak detection in various experimental techniques including Raman Spectroscopy [10] and X-ray diffraction [11]. The strength of this baseline subtraction scheme is that it can provide consistent results, even with many overlapping peaks, with minimal user input. In this work, an iterative algorithm based on the multi-level discrete wavelet transform is presented to remove unwanted signals from UED data.

3.4.1 The Discrete Wavelet Transform

The discrete wavelet transform decomposes functions into a basis of wavelets, derived from a mother wavelet. Intuitively, the mother wavelet is chosen to be localized in both frequency and space. These requirements imply functions of zero-mean, resulting in oscillating behaviour, and giving the name *wavelets*.

The basis of wavelets $\{\psi_{jk} : j, k \in \mathbb{Z}\}$ is defined as the set of dilations and translations of the mother wavelet ψ :

$$\psi_{jk}(x) = 2^{j/2}\psi(2^j x - k) \quad (3.3)$$

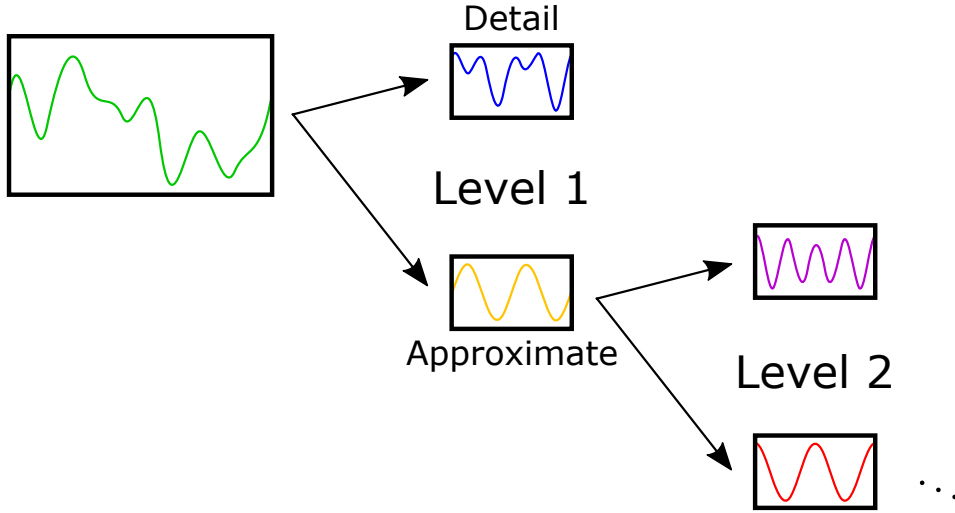


FIGURE 3–8: Diagram of the Mallat algorithm for the multi-level discrete wavelet transform. The original signal (left, green) is decomposed into a set of approximate coefficients (top, blue) and a set of detail coefficients (bottom, yellow). Further decomposition levels are iteration of the previous procedure on the approximate coefficients.

The finite support in the frequency and space domains gives the wavelet transform local information, something that is not possible with the Fourier transform due to the non-compactness of sines and cosines in space [12].

The discrete wavelet transform, as implemented in Mallat's algorithm, is a convolution cascade of filter banks [13]. The mother wavelet is decomposed into two filters: a high-pass filter and a low-pass filter, the derivation of which is beyond the scope of this work. These filters are stretched and translated before being convolved with a data signal. The remaining coefficients at each scale and position give the wavelet representation of the data signal, known as coefficients.

The decomposition of a data signal in low-frequency (approximate) coefficients and high-frequency (detail) coefficients represents one level of transform. Further decomposition is done by iteratively transforming the approximate coefficients until the scaled wavelets are

longer than the number of coefficients. This iteration is known as the *multi-level discrete wavelet transform*, of which a diagram is shown on Fig. 3–8, and is the basis of the baseline-removal algorithm that is presented herein.

3.4.2 An Iterative Algorithm

The algorithm is an iterative computation of baselines that are modified until convergence. During each iteration, an approximate baseline is determined via the multi-level discrete wavelet transform. The detail (read: high-frequency) coefficients are then rejected, and only the approximate coefficients are kept.

This approximate baseline contains some information from the elastic scattering peaks, and therefore will be larger than the raw signal in some data regions. To negate the influence of the elastic scattering peaks on the background determination, the approximate baseline is modified so that it does not exceed the raw signal anywhere. In addition, if data regions exclusively composed of background were specified, the approximate baseline is set to be equal to the raw signal in these regions. This modified approximate baseline is then fed to the next iteration. Due to the smaller impact of elastic scattering peaks at each subsequent iteration, the algorithm converges to a baseline. The effect of iteration is displayed on fig. Fig. 3–9 [10].

Apart from the choice of mother wavelet, the only parameter requiring user intervention is the decomposition level. The decomposition level depends on the frequency components of the raw signal, and, incidentally, on the length of the (discrete) raw signal.

3.4.3 Testing via simulations

The validity of this approach is tested by simulating powder diffraction patterns of VO₂ transitioning from monoclinic M1 to rutile. The phase transition is simulated to happen at an exponential rate, with a time-constant of 200 fs. A static background is added, in

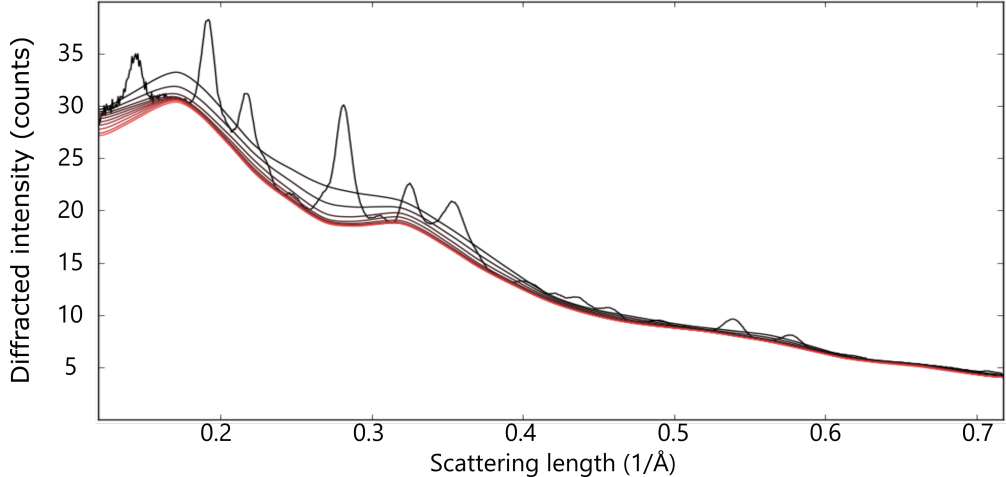


FIGURE 3–9: Effect of iteration in baseline determination on real data. The algorithm converges quickly to a baseline.

the form of a biexponential function with two gaussian-shaped 'humps' typical of sample substrates used in Morrison et al. [5]. The simulated experiment is presented in Fig. 3–10.

The baseline identification is done on the powder diffraction pattern at photoexcitation ($t = 0$), with the sample being entirely monoclinic M1. This baseline is subtracted from the simulated patterns at all time points. The resulting reconstructed patterns are shown on fig. Fig. 3–11, including the residuals between the known diffraction patterns without background, and their reconstructions.

The dynamics of diffraction peaks is most important, beyond whole-pattern reconstruction. Time-scales of diffraction intensities changes is an important quantity in ultrafast electron diffraction experiments [5, 14]. Fig. 3–11 highlights some characteristic peaks of the phase transition in VO₂. The average time-constant in the amplitude change of the peaks marked by black lines in Fig. 3–11 was found to be (200 ± 20) fs, as set in the simulation parameters. This simulation shows that the recovered dynamics are not warped by the baseline-removal.

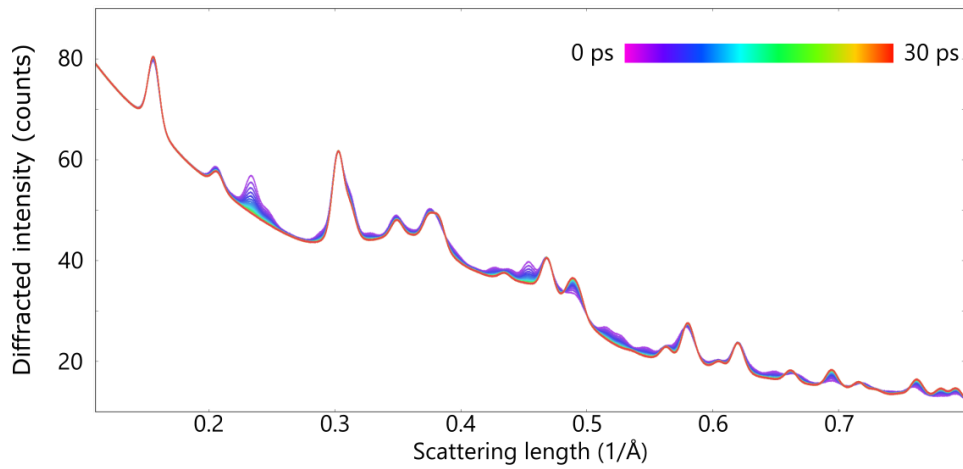


FIGURE 3–10: Simulated experiment showcasing a phase transition of VO₂ from monoclinic M1 (purple) to rutile (red). The phase transition speed has an exponential time constant of 200 fs. A static background is added.

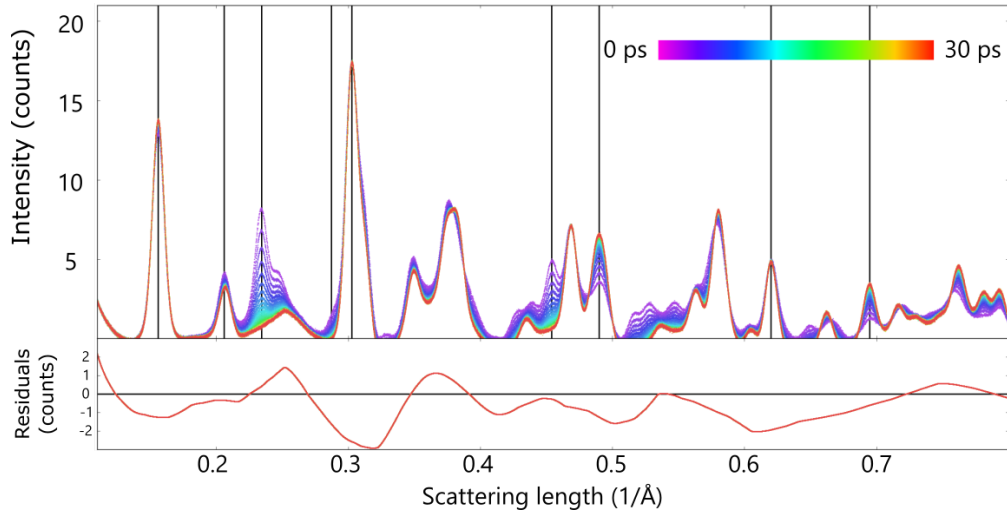


FIGURE 3–11: **Top:** baseline-subtracted diffraction patterns from Fig. 3–10. Characteristic peaks of the phase transition are highlighted by black lines. The time-constant of the intensity change at those characteristic peaks averages (200 ± 20) fs, in agreement with the simulation parameter of 200 fs. **Bottom:** residuals between the known diffraction patterns and their reconstruction.

References

- [1] Bradley J. Siwick, Jason R. Dwyer, Robert E. Jordan, and R. J. Dwayne Miller. Ultrafast electron optics: Propagation dynamics of femtosecond electron packets. *Journal of Applied Physics*, 92(3):1643–1648, 2002.
- [2] T. Van Oudheusden, E. F. De Jong, S. B. Van Der Geer, W. P E M Op 'T Root, O. J. Luiten, and Bradley John Siwick. Electron source concept for single-shot sub-100 fs electron diffraction in the 100 keV range. *Journal of Applied Physics*, 102(9), 2007.
- [3] Vance R. Morrison. *Structural dynamics of the metal-insulator transition in VO₂: an ultrafast electron diffraction study with radio-frequency compressed electron pulses*. PhD thesis, McGill University, 2014.
- [4] W.I.F. David, K. Shanklannd, L.B. McCusker, and Ch. Baerlocher. *Structure determination from powder diffraction data*. Oxford University Press, New York, 2002.
- [5] Vance R. Morrison, Robert P. Chatelain, Kunal L Tiwari, Ali Hendaoui, Andrew Bruhacs, Mohamed Chaker, and Bradley John Siwick. A photoinduced metallic phase of monoclinic VO₂ revealed by ultrafast electron diffraction. *Science*, 341(6208):19, 2014.
- [6] M. Jarvinen. Application of symmetrized harmonics expansion to correction of the preferred orientation effect. *Journal of Applied Crystallography*, 26(pt 4):525–531, 1993.
- [7] Catherine Kealhofer, Stefan Lahme, Theresa Urban, and Peter Baum. Signal-to-noise in femtosecond electron diffraction. *Ultramicroscopy*, 159(P1):19–25, 2015.

- [8] Bradley John Siwick. *Femtosecond Electron Diffraction Studies of Strongly-Driven Structural Phase Transitions*. PhD thesis, University of Toronto, 2004.
- [9] Fengkui Zhao and Aimin Wang. A background subtraction approach based on complex wavelet transforms in EDXRF. *X-Ray Spectrometry*, 44(2):41–47, 2015.
- [10] C. M. Galloway, E. C. Le Ru, and P. G. Etchegoin. An iterative algorithm for background removal in spectroscopy by wavelet transforms. *Applied Spectroscopy*, 63(12):1370–1376, 2009.
- [11] John M. Gregoire, Darren Dale, and R. Bruce van Dover. A wavelet transform algorithm for peak detection and application to powder x-ray diffraction data. *The Review of scientific instruments*, 82(1):015105, jan 2011.
- [12] Ingrid Daubechies. The wavelet transform, time-frequency localization and signal analysis. *Information Theory, IEEE Transactions on*, 36(5):961–1005, 1990.
- [13] Stephane G. Mallat. A Theory for Multiresolution Signal Decomposition: The Wavelet Representation. *IEEE Transactions on Pattern Analysis and Machine Intelligence*, 11(7):674–693, 1989.
- [14] Robert P. Chatelain. *Radio-frequency pulse compression for high-brightness ultrafast electron diffraction : design, characterization and application*. PhD thesis, McGill University, 2014.

CHAPTER 4

Scattering Potential Maps and a Photoinduced Metal-like Phase of VO₂

This chapter describes a processing technique for ultrafast diffraction data that allows us to calculate the time-dependence of the scattering potential $V(\mathbf{r})$. This analysis tool is more intuitive than reciprocal-space-based techniques such as the Patterson function.

In subsequent sections, this technique is applied to the diffraction data presented by Morrison et al. [1].

4.1 From Data to Scattering Potential Maps

The objective of this section is to go through the computational details of building a scattering potential map, described in Chapter 2. While it is a simple calculation (see Eq. 2.8), some quantities (e.g. diffraction phase) must be calculated from a known crystal structure.

The equation relating measurable diffraction quantities to the scattering potential was presented in Chapter 2 as Eq. 2.8. It is reproduced below for convenience:

$$\phi(\mathbf{r}, t) = \sum_{\{\mathbf{G}\}} |S(\mathbf{G}, t)| e^{i\chi(\mathbf{G}, t)} \cos(\mathbf{G} \cdot \mathbf{r}) \quad (4.1)$$

where $\phi(\mathbf{r}, t)$ is the scattering potential in real space and $\chi(\mathbf{G}, t)$ is the phase of the (generally complex) structure factor $S(\mathbf{G}, t)$, $|S(\mathbf{G}, t)| = \sqrt{I(\mathbf{G}, t)}$.

4.1.1 Diffracted Intensity

The first step in calculating the scattering potential is to extract the diffracted intensity $I(\mathbf{G}, t)$ for all relevant scattering vectors \mathbf{G} . The allowed scattering vectors depend on the crystal structure, and thus the intensity extraction is sped up by only looping over the scattering vectors allowed by the space group symmetry.

Decomposing the diffraction data for various scattering vectors is no simple task when using polycrystalline samples. Since data is taken as a function of $|\mathbf{G}|$, a diffraction peak can carry intensity contributions from as many as 30 scattering vectors in the case of VO_2 , when peak broadening is taken into account.

A common algorithm to extract intensities is the Le Bail method, which operates with no assumption on the crystal structure [2]. Unfortunately, a lot of characteristic VO_2 diffraction peaks have too much overlap for the Le Bail method to work reliably. Again, the solution is to make use of the (known) crystal structure of VO_2 . A diffraction powder pattern is simulated, and the relative contribution for each scattering vector \mathbf{G} is recorded. This relative contribution is introduced into the computation as a correction factor to the intensity $I(\mathbf{G}, t)$.

4.1.2 Diffraction Phase from Structure Factors

In general, recovering the scattering factor phase from diffraction data *ab initio* is a difficult problem and falls outside the scope of this work. A description of the problem is presented by W.I.F. David et al. [3]. Fortunately, in the specific case of VO_2 , it is possible to infer what the diffraction phases are from the initial monoclinic M1 structure of the material. The second term of Eq. 4.1, the diffraction phase $e^{i\chi(\mathbf{G}, t)}$, can be computed using the crystal

structure and the atomic form factors for each atom. While the crystal structure for VO_2 is straightforward to implement, the atomic structure factors for V and O are modeled from [4] as a sum of Gaussian functions:

$$f_j(\mathbf{G}) = \sum_{i=1}^5 a_i e^{-b_i s^2} \quad (4.2)$$

for $4\pi s = |\mathbf{G}|$. Factors $\{a_i\}$ and $\{b_i\}$ are listed in Table 4.3.2.2 of [4]. Then, the phase $\chi(\mathbf{G}, t)$ is taken as the signed polar angle of the (complex) structure factor $S(\mathbf{G}, t)$:

$$\chi = \text{atan2}(\text{Im}(S), \text{Re}(S)) \quad (4.3)$$

where atan2 is the two-argument arctangent function, which computes the arctangent and its sign depending on the sign of the input.

4.2 Testing on Static Diffraction Data

This section describes the validity of scattering potential maps, tested using static powder ultrafast electron powder diffraction data. The data used is the average of the powder diffraction patterns at a photoexcitation fluence of 9 mJ/cm^2 of Morrison et al. [1] before photoexcitation, when the sample is in the monoclinic M1 phase. This data is plotted in Fig. 4–1.

The equilibrium scattering maps for two orientations is shown on Fig. 4–2. These two orientations are perpendicular to each other, with their intersection overlaid as a dashed red line. The top map shows a cut of the scattering potential along the \mathbf{c}_R -axis, passing through the middle of the oxygen octahedra. Red overlays show two perpendicular projections of the oxygen octahedra in a single map. In this geometry, the oxygen atoms are clearly seen as positive, surrounding the much more positive vanadium atoms. These vanadium atoms form tilted dimerized chains, highlighted by the linear cuts shown by green and yellow dashed line, as well as a blue overlay. The tilting axis alternates by 90 deg for each chain: some

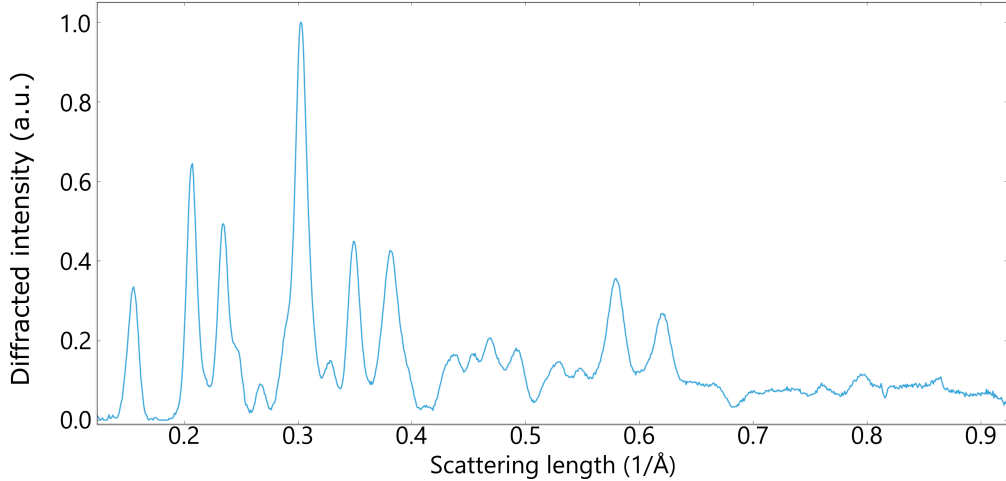


FIGURE 4–1: Electron diffraction data for polycrystalline sample of VO_2 , averaged over times before photoexcitation.

vanadium chains are tilted completely in the plane of the page, while other vanadium chains appear untilted because the tilt axis is parallel to the page. The top map is coplanar with the angular part of the $d_{x^2-y^2}$ orbital: note that $\hat{\mathbf{x}} \parallel \mathbf{c}_R$ and $\hat{\mathbf{y}} \parallel \mathbf{a}_R + \mathbf{b}_R$, as presented in Fig. 1–2.

The bottom map is intersects the top map at the red dashed line, but cuts perpendicularly to the V – V chains. This plane (and the associated linear cuts) focuses on the oxygen atoms: we can see a slight distortion from a perfect octahedron by following the dashed lines across the map. The oxygen octahedron are all oriented in the same direction, as shown with red overlays. The bottom map is coplanar with the angular part of the d_{yz} orbital (see Fig. 1–2).

4.2.1 Comparison of Radial Pair-distribution Functions

As described in Section 2.4, the radial pair-distribution function (PDF) is an essential tool in the analysis of powder diffraction data, as it can be computed directly from diffraction intensities. As the PDF is the autocorrelation of the scattering potential, maximas in radial PDFs represent inter-atomic distances. Comparing the radial PDF derived from diffraction

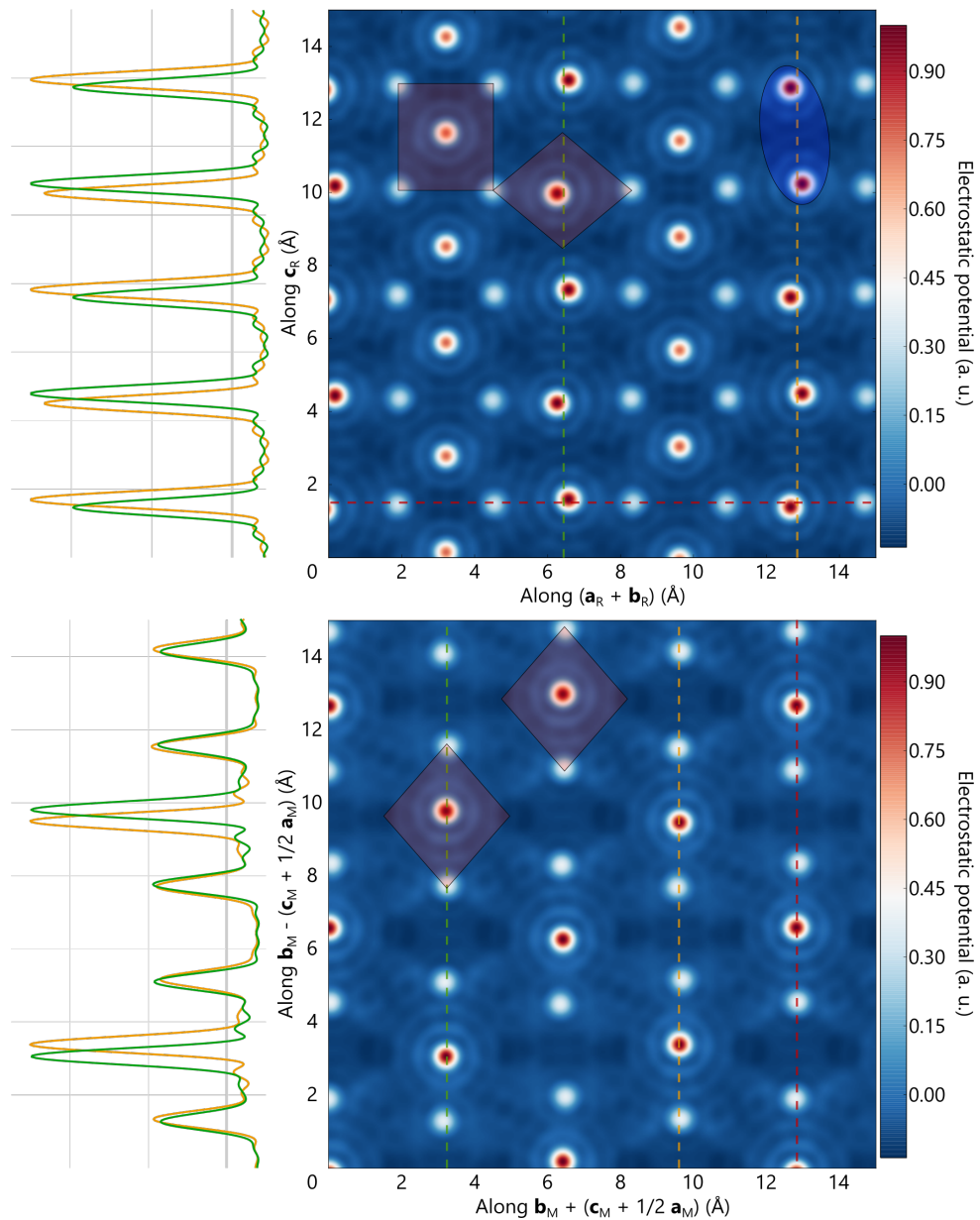


FIGURE 4–2: Scattering potential map of equilibrium monoclinic M1 VO₂. Both maps intersect at the red dashed line. Linear cuts are taken to highlight features. **Top:** scattering potential map cutting through the V – V dimers (blue overlay), characteristic of the monoclinic M1 VO₂ crystal structure. Two non-equivalent orientations of the oxygen octahedra are shown in red overlay. **Bottom:** scattering potential map perpendicular to the vanadium dimers. The oxygen octahedra (red overlays) are all oriented in the same direction

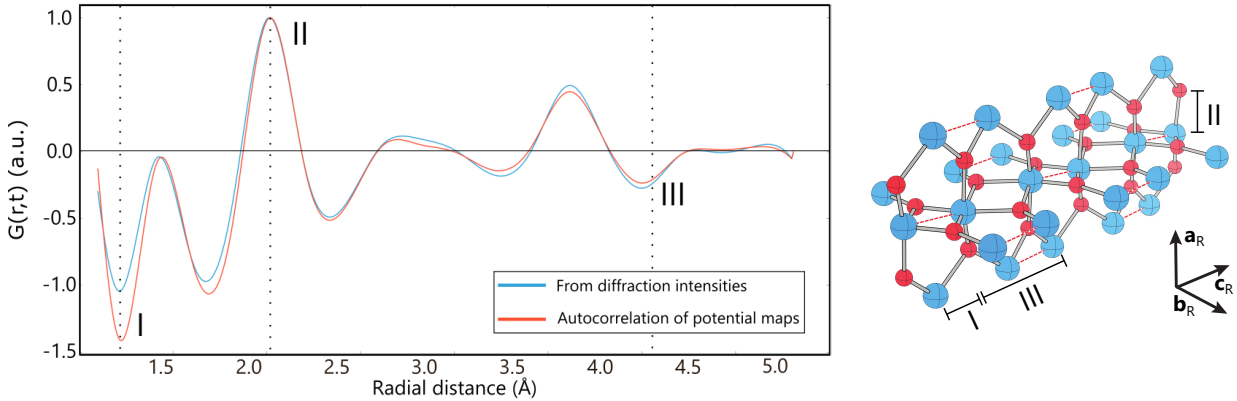


FIGURE 4–3: **Left:** average radial pair-distribution function $G(r, t)$ of times before photoexcitation, computed in two ways from the same data. Highlighted extrema represent inter-atomic distances shown on the right. **Right:** monoclinic M1 structure of VO_2 .

intensities alone to the radial PDF calculated from a scattering potential volume should reveal how robust the structure factor phase estimation and diffraction intensities distribution are.

Fig. 4–3 displays such a comparison. A scattering potential volume has been computed for the equivalent of 8 unit cells from the diffraction data shown on Fig. 4–1, and the autocorrelation of this volume was radially-averaged. The radial PDF was directly computed from the diffraction intensities as well.

The radial PDF of Fig. 4–3 shows a number of extrema, and some characteristic interatomic distances are worth pointing out. The positive feature around 2 \AA (II) is the average $\text{V} - \text{O}$ distance in the octahedron. The negative feature at 1.3 \AA (I) is due to half of the $\text{V} - \text{V}$ dimer bond length, and the negative feature at 4.4 \AA (III) represents the undimerized $\text{V} - \text{V}$ distance plus half of the $\text{V} - \text{V}$ bond length. These features will be important in the analysis of the time-resolved data in subsequent sections.

The two compared radial PDFs display excellent qualitative agreement; this implies that the calculations of diffraction phases, as well as the distribution of diffraction intensities, are

valid approximations. While the scattering potential maps are consistent with the radial PDF approach, they go further by showing local information, which makes the interpretation of results much more natural and immediate.

4.3 A Photoinduced Metal-like Phase of Monoclinic VO₂

Morrison et al. [1] describes the discovery of a new photoinduced phase of VO₂ with metal-like infrared transmission properties, with the monoclinic M1 structure.

Above a threshold pump laser fluence, photoexcitation induces an increase in crystallographic symmetry, with an effecting halving of the VO₂ unit cell. This is the typical nonthermal melting of the monoclinic M1 VO₂ structure to rutile VO₂ as first referenced in [5]. However, by photoexciting below the threshold laser pump fluence, a metastable state (lifetime >100 ps) with no crystallographic changes from the monoclinic insulating phase is reached. While the equilibrium monoclinic phase is insulating, this new monoclinic phase has metal-like infrared transmittance. The results are graphically presented in Fig. 4–4.

The time-resolved powder diffraction pattern shows a fast (\sim 310 fs) time-scale and a slow (\sim 1.6 ps) time-scale, on panels Fig. 4–4 B and E respectively. These dynamic features are reported to be independent, since below a threshold photoexcitation fluence of 9 mJ cm⁻², only the slower dynamics are observed.

The time-scales are found on different diffraction peaks. The fast changes are seen in peaks associated with the thermal melting of monoclinic M1 VO₂ to rutile VO₂: most notably, peaks (30 $\bar{2}$), (12 $\bar{2}$), and (31 $\bar{3}$) fade away with a fluence-dependent intensity change (Fig. 4–4 panel D). On the other hand, the slow dynamics affect a whole range of scattering vectors. These slow changes do not point to a structural phase transition as the structure stays monoclinic M1 for at least 500 ps. The slow dynamics are not observed in reflections whose reciprocal lattice vector is perpendicular to \mathbf{c}_R (gray lines in Fig. 4–4 panel A). This

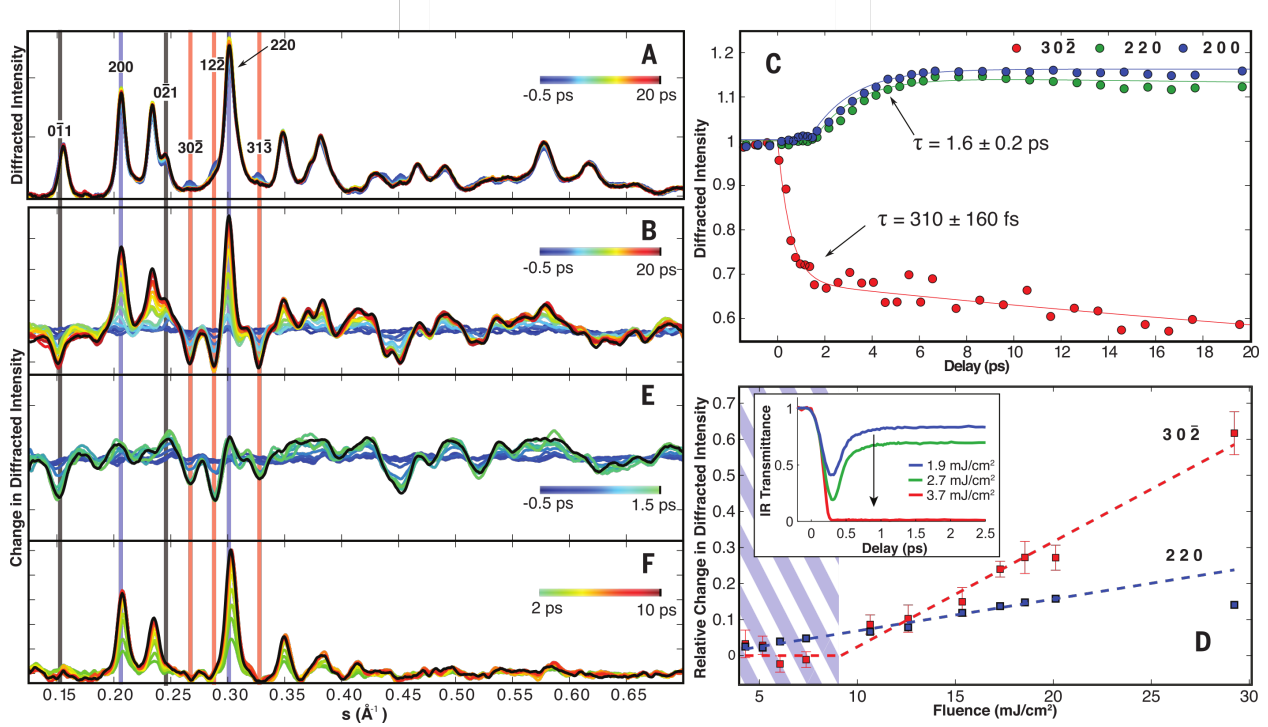


FIGURE 4-4: Structural dynamics during the insulator-metal transition in VO₂. **A:** Background-subtracted ultrafast electron diffraction data from 0 to 20 ps. Red vertical lines indicate some reflections that are allowed in the M1 structure, but not in R. Blue vertical lines indicate reflections that are allowed in both M1 and R. Gray vertical lines indicate peaks that are associated with the crystallographic direction perpendicular to \mathbf{c}_R (\mathbf{a}_M). **B:** Difference diffraction pattern from -0.5 to 20 ps. **C:** Time-resolved diffraction peak intensity showing fast (310 fs) and slow (1.6 ps) dynamics, respectively, for peaks indicated by red and blue vertical lines in (A), (B), (E), and (F). **D:** Fluence dependent of the fast and slow signal amplitudes as measured from (30̄2) and (220) peaks shown in (C). The range of fluences for which no phase transition is observed is indicated by hatched region. Inset: time-resolved IR (5 μm , 0.25 eV) transmissivity in the hatched fluence region displays a persistent decrease to a very long-lived plateau (>100 ps). The amplitude of this decrease reaches > 99% at 3.7 mJ cm^{-2} , indicating a closing of the semiconducting gap and a transition to a metallic-like state. **E:** Difference diffraction pattern for fast dynamics, showing nonthermal melting of the M1 structure into rutile. **F:** Difference diffraction pattern for slower dynamics, showing no changes in crystallographic structure. Between 3 and 9 mJ cm^{-2} pump fluence, only these changes are observed. Figure reproduced from [1] with permission. **F:** Diffraction difference spectrum for the slow dynamics. The change in diffracted intensity from 2 to 10 ps (referenced to 2 ps) is shown. Figure reproduced with permission from [1].

implies that the slow dynamics are due to a 1D change in electrostatic potential along the \mathbf{c}_R -axis.

4.4 The Structure of the Photoinduced Monoclinic Metal-like State of VO₂ via Scattering Potential Maps

As previously stated, the scattering potential maps is a tool facilitating analysis of structural and electronic dynamics in powder diffraction. The techniques of previous sections were applied to the 9 mJ/cm² fluence diffraction data presented in Fig. 4–4 (panel F). The results are presented on Fig. 4–5. The maps represent the same two perpendicular planes that were used to produce Fig. 4–2. The difference in scattering potential shows the map at a time-delay of 10 ps, referenced at 2 ps, after the fast transition of some crystallites to the rutile structure.

The qualitative maps shown on Fig. 4–5 are consistent with the conclusions of Morrison et al. [1]. The change in scattering potential from Fig. 4–5 is purely due to electronic reorganization; the position of the vanadium and oxygen atoms is invariant: the structure shown on Fig. 4–5 possesses the crystallographic symmetry of monoclinic M1 VO₂. The scattering potential maps also display strengthening of the bonding between vanadium dimers that was deduced from the absence of diffraction intensity changes for certain reflections (e.g. (0 $\bar{1}$ 1) and (02 $\bar{1}$)).

Fig. 4–6 shows the change radial PDFs $\Delta G(r, t)$ computed with the diffraction data at 10 ps (referenced at 2 ps) using a direct method, and using the autocorrelation of scattering potential volumes. The positive feature at 2 Å (II), the average V – O bond length, shows a an increase in electrostatic potential (equivalently, decrease in electron density) at the oxygen atoms. The negative features at 1.3 Å (I) and 4.4 Å (III), related to the V – V bond lengths, indicate that this change in electrostatic potential on the oxygen atoms acts to favour the V – V dimers strength. This observation is also visible in the scattering maps, although not

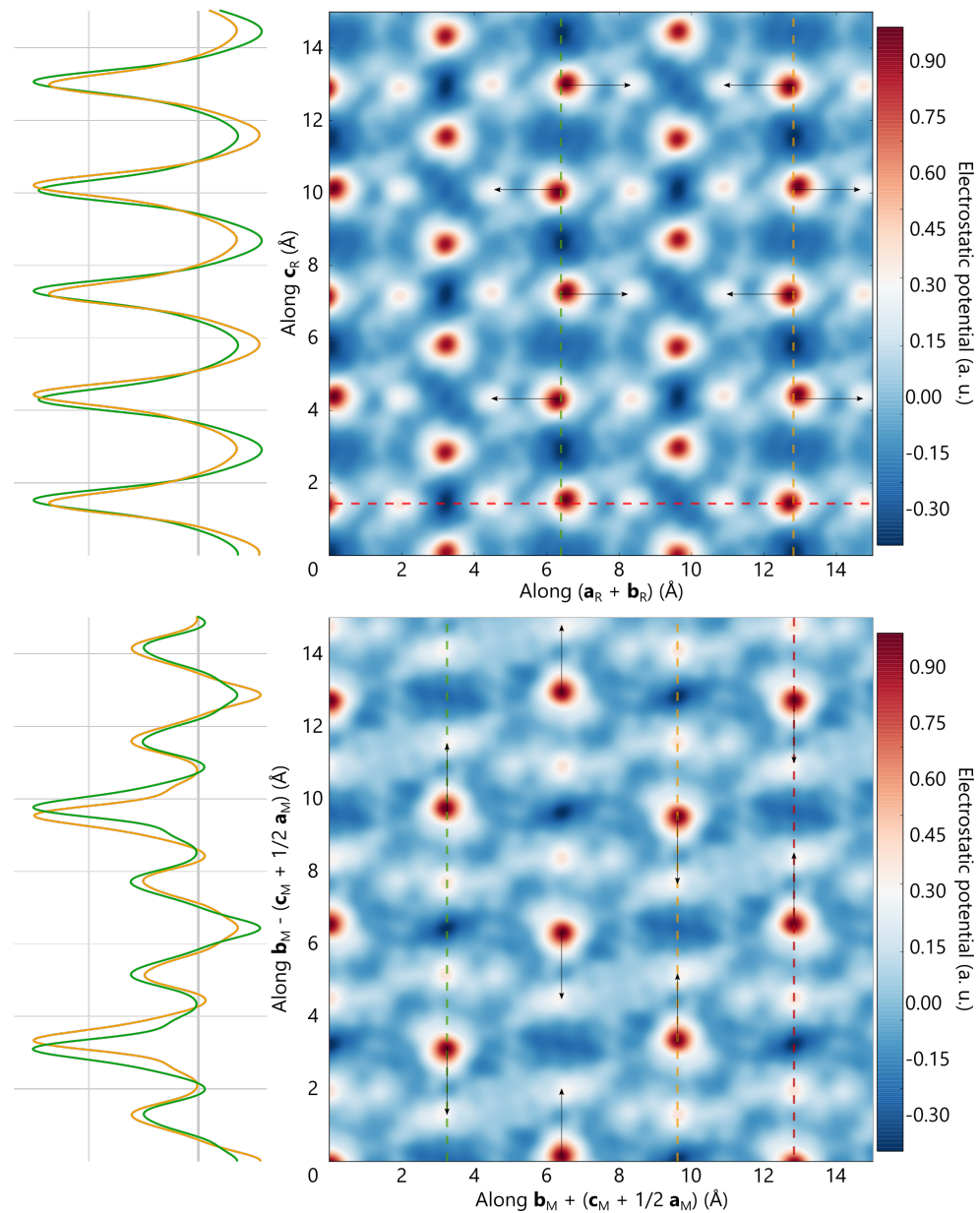


FIGURE 4–5: Electrostatic potential map computed from difference intensity data of 10 ps (referenced at 2 ps). The planes are equivalent orientations to Fig. 4–2. Both vanadium and oxygen atoms grow more positive as the electrons move to reinforce the charge-density wave. Changes in the electrostatic potential follows an anti-ferroelectric pattern, highlighted by arrows. **Top:** difference electrostatic potential along the oxygen place. **Bottom:** difference electrostatic potential along the unit cell floor, oriented along the solid red line through the page.

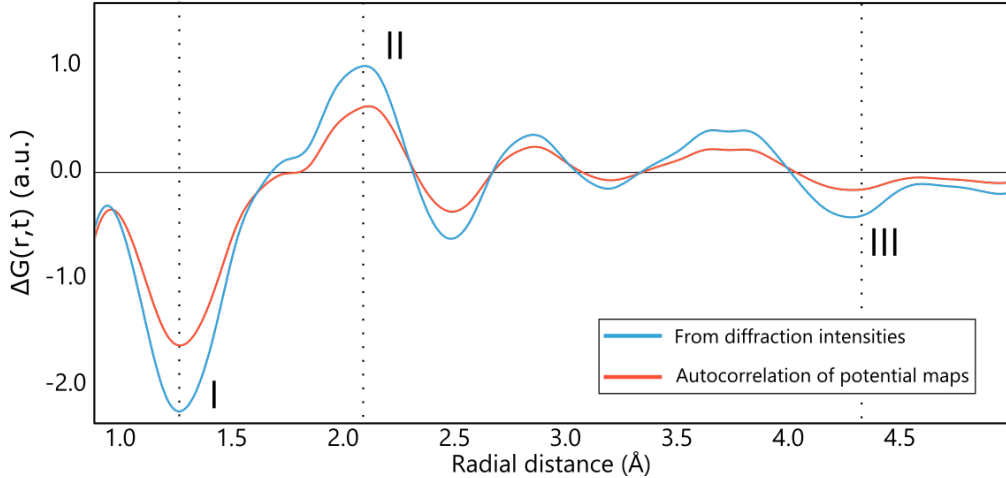


FIGURE 4–6: Change in the radial pair-distribution function $\Delta G(r,t) = G(r, 10\text{ ps}) - G(r, 2\text{ ps})$. Highlighted extrema represented inter-atomic distances shown on Fig. 4–3.

all oxygen atoms are affected equally. This figure shows that the scattering potential maps of the slow dynamics are consistent with results presented by [1].

However, the scattering potential maps of Fig. 4–5 contain more information than is apparent from the diffraction patterns alone. The information provided by the maps is local, and is therefore superior to radial pair-distribution function analyses. This fact makes it easier to compare experimental data with simulations directly. Fig. 4–5 shows that the change in electrostatic potential follows an anti-ferroelectric pattern, highlighted by black arrows. This new information is not accessible to analyses by radial PDFs, and will be discussed in the next section.

4.5 Discussion with a Theoretical Perspective

A recent publication by He and Millis [6] attempts to explain the emergence of a metastable metallic monoclinic M1 phase of VO_2 , as reported by Morrison et al. [1] and introduced in Section 4.3. The scattering potential maps are an ideal tool to investigate the validity of the authors' claims.

A density functional theory method was used in the computation of partial band structures of VO_2 . This method includes on-site and inter-site interaction energies U and V , respectively, treated by a Hartree-Fock approach. The interaction energies U and V were kept within a physically reasonable range ($3.5 \text{ eV} \leq U \geq 4.5 \text{ eV}$ and $0.6 \text{ eV} \leq V \geq 1.4 \text{ eV}$).

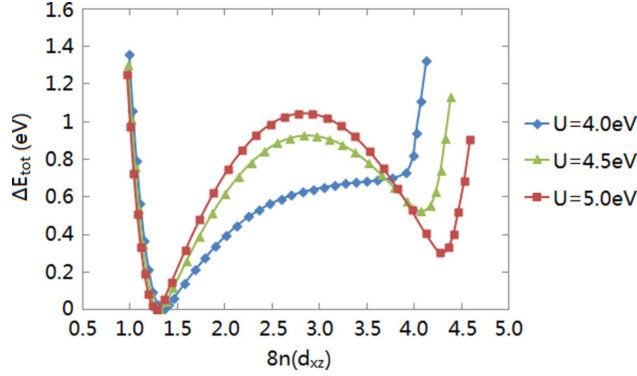


FIGURE 4–7: Energy landscape of monoclinic VO_2 at different values of U and with $V = 1 \text{ eV}$ fixed, as a function of d_{xz} orbital occupancy. A local minima corresponding to a metallic metastable state is present for $U \geq 4.5 \text{ eV}$. Reproduced from [6] with permission.

The energy landscape as a function of d_{xz} orbital occupancy is plotted in Fig. 4–7 for variations in the on-site interaction energy U . The crystal structure is fixed in monoclinic M1. The authors report that within their framework, for parameters $U \geq 5 \text{ eV}$ and $V = 1 \text{ eV}$, the system can be prepared in a metastable state with no band gap at the Fermi level. The emergence of this metastable state’s metallic character is due to a high d_{xz} – and low $d_{x^2-y^2}$ – orbital occupancy. Fig. 4–8 compares the (partial) energy band diagrams for equilibrium (insulating) monoclinic M1 VO_2 , and its metastable metallic state. The population inversion between d_{xz}/d_{yz} and $d_{x^2-y^2}$ is apparent, and occurs when the overlap of the $d_{x^2-y^2}$ band with the d_{xz}/d_{yz} bands exceeds a certain threshold; the new energy ordering, with the d_{xz}/d_{yz} bands sitting at lower energy, creates this metallic phase.

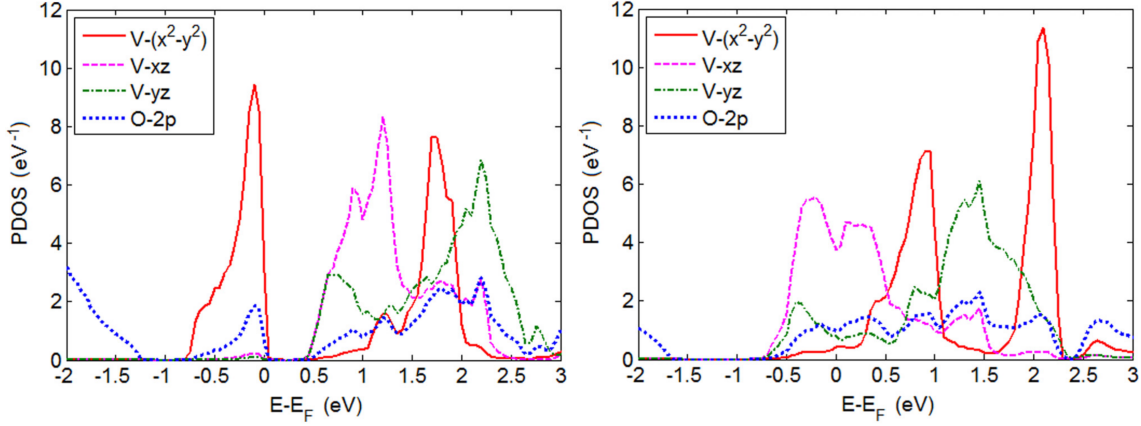


FIGURE 4–8: **Left:** simulated partial energy band diagram of the equilibrium (insulating) monoclinic M1 VO₂ phase. **Right:** simulated partial energy band diagram of the metastable phase of VO₂ ($U = 4.5$ eV, $V = 1$ eV) shows no gap at the Fermi level. Reproduced from [6] with permission.

This stands in contrast with lower interaction parameters U and V . For $U = 4$ eV and $V = 1$ eV, the band $d_{x^2-y^2}$ shifts up and the d_{xz}/d_{yz} bands shift down with temperature, eventually closing the gap at the Fermi level, without undergoing a phase transition.

This *monoclinic metal* is not thermally accessible, as it is not a global energy minima, but the population inversion between the d_{xz} and $d_{x^2-y^2}$ bands can be driven by photoexcitation. Fig. 4–9 shows that for appropriate values of U and V , the Fermi level band gap E_{gap} can be closed via a first-order phase transition by injecting enough energy per unit cell ΔE_{tot} .

Comparison with Scattering Potential Maps

This section discusses the results from He and Millis, in light of the scattering potential maps presented in Section 4.4. The depopulation of the $d_{x^2-y^2}$ band in favour of the d_{xz} band could result in an anti-ferroelectric pattern [8]. This is suggested in the scattering potential maps, as highlighted by arrows in Fig. 4–5; not all oxygen atoms are affected equally by

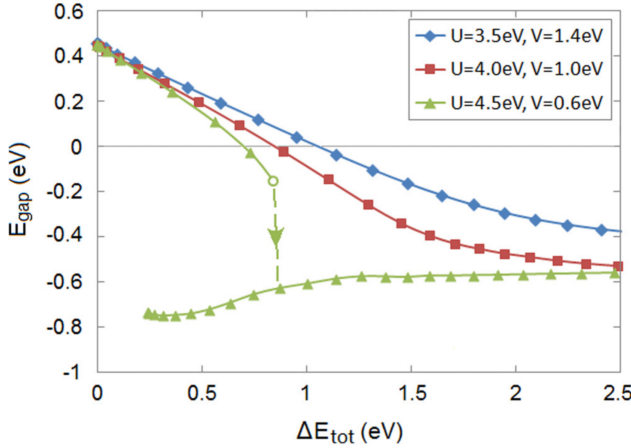


FIGURE 4–9: Energy gap E_{gap} as a function of energy injected per unit cell by the laser pulse under various parameters U and V . Adapted from [6] with permission.

the overall increase in electrostatic potential. This new information was not accessible using radial PDFs as the primary analysis tool.

The primary feature of the scattering potential maps, the strengthening of the $V - V$ dimer bonds, remains puzzling. The author is not yet in a position to explain the appearance of this 1D *charge-density wave* and how it relates to the change in properties between the insulating and metallic phases of monoclinic M1 VO_2 . It is possible that the correlated electronic states in insulating monoclinic M1 (with a highly occupied $d_{x^2-y^2}$ band) puts less electron density than the uncorrelated electronic states of the metallic monoclinic M1 state, with a high occupancy in the d_{xz} band. Further work is required in order to compare the predictions of He and Millis with the maps presented in Fig. 4–5.

References

- [1] Vance R. Morrison, Robert P. Chatelain, Kunal L Tiwari, Ali Hendaoui, Andrew Bruhacs, Mohamed Chaker, and Bradley John Siwick. A photoinduced metallic phase of monoclinic VO_2 revealed by ultrafast electron diffraction. *Science*, 341(6208):19, 2014.
- [2] Armel Le Bail. Whole powder pattern decomposition methods and applications: A retrospection. *Powder Diffr.*, 20(04):316–326, 2005.
- [3] W.I.F. David, K. Shanklannd, L.B. McCusker, and Ch. Baerlocher. *Structure determination from powder diffraction data*. Oxford University Press, New York, 2002.
- [4] J.M. Cowley. Scattering factors for the diffraction of electrons by crystalline solids. In Theo Hahn, editor, *International Tables for Crystallography*, volume A, chapter 4, pages 259–429. Kluwer Academic Publishers, New York, third edit edition, 2006.
- [5] A. Cavalleri, H.H.W. Chong, R.W. Schoenlein, J.C. Kieffer, and Th. Dekorsy. Structural bottleneck in the photo-induced insulator to-metal transition in VO_2 . *Physical Review B*, 70, 2004.
- [6] Zhuoran He and Andrew J. Millis. Photoinduced phase transitions in narrow-gap Mott insulators: the case of VO_2 . *Physical Review B*, 93(11), 2015.
- [7] Volker Eyert. The metal-insulator transitions of VO_2 : A band-theoretical approach. *Ann. Phys. (Leipzig)*, 11:650–702, 2002.
- [8] RM Wentzcovitch, WW Schulz, and PB Allen. VO₂: Peierls or Mott-Hubbard? A view from band theory. *Physical review letters*, 72(21):3389–3392, may 1994.

Conclusion

In summary, the development of new analysis tools for ultrafast electron diffraction has been demonstrated. These tools extend the capabilities of ultrafast electron diffraction, and accelerate data processing and analysis.

The scattering potential maps are a transparent representation of structural and electronic reorganizations in crystals. Combined with electron diffractions high sensitivity to changes in valence charge distribution, this technique can be used to investigate dynamics in orbital occupancy and orbital/charge order in strongly-correlated materials. The combination of ultrafast electron diffraction and scattering potential maps should be seen as a powerful probe of electronic structure, not only lattice structure in condensed matter. This new technique was shown to be consistent with previous results by Morrison et al. [1], as well as offer information that could be compared directly with DFT calculations such as He and Millis [2].

A robust baseline-removal algorithm was also developed to accelerate data analysis. This iterative algorithm was shown to perfectly extract diffraction dynamics in simulated experiments. The baseline-removal routine is much more stable than typical curve-fitting or interpolation techniques, as well as being much faster.

Outlook

The scattering potential maps shows significant improvement over previous elementary analysis techniques, but the work is far from over. The specific case of a known structure (monoclinic M1 VO₂) makes the computation of diffraction phases trivial, but there is no hard requirement of known structures other than for phase computation; it would be possible to experimentally determine the diffraction phases using convergent beam electron diffraction (CBED), for example.

Baseline-removal using the discrete wavelet transform is a hot topic in experimental science. Recent advances in the dual-tree complex wavelet transform [3] will form the basis of next-generation data processing tools. The extension of the algorithm described in this thesis to use the dual-tree complex wavelet transform should be straightforward.

Another planned upgrade of the baseline-removal algorithm that is the ability track the dynamics of the inelastic scattering, as well as diffraction from the substrate. Since the wavelet approach is much faster than curve-fitting routines, it is now possible to process the background for each time-delay individually. Removing the influence of the background diffraction effects from the elastic scattering data could boost the signal-to-noise ratio and reveal new phenomena that has been buried in the data.

References

- [1] Vance R. Morrison, Robert P. Chatelain, Kunal L Tiwari, Ali Hendaoui, Andrew Bruhacs, Mohamed Chaker, and Bradley John Siwick. A photoinduced metallic phase of monoclinic VO₂ revealed by ultrafast electron diffraction. *Science*, 341(6208):19, 2014.
- [2] Zhuoran He and Andrew J. Millis. Photoinduced phase transitions in narrow-gap Mott insulators: the case of VO₂. *Physical Review B*, 93(11), 2015.
- [3] Fengkui Zhao and Aimin Wang. A background subtraction approach based on complex wavelet transforms in EDXRF. *X-Ray Spectrometry*, 44(2):41–47, 2015.

APPENDIX A

Structural Parameters of VO₂ Crystal Phases

The following structural description of the crystalline phases of VO₂ are taken from Eyert [1]. It is reproduced here for reference.

Below 70 °C, VO₂ crystals exhibit the monoclinic M1 structure with a doubling of the unit cell size. Vanadium atoms are no longer evenly spaced: dimerization occurs along the rutile **a**₃-axis. The monoclinic M1 lattice vectors are given by:

$$\begin{pmatrix} \mathbf{a} \\ \mathbf{b} \\ \mathbf{c} \end{pmatrix}_{M1} = \begin{pmatrix} 0 & 0 & -5.742 \\ -4.517 & 0 & 0 \\ 0 & 4.526 & -2.900 \end{pmatrix} \begin{pmatrix} \hat{\mathbf{e}}_1 \\ \hat{\mathbf{e}}_2 \\ \hat{\mathbf{e}}_3 \end{pmatrix} \quad (\text{A.1})$$

At atmospheric pressure and above 70 °C, VO₂ crystals have a tetragonal rutile (R) structure with a unit cell composed of 6 atoms. The rutile lattice vectors are represented by a proper normalization of the standard cartesian basis { $\hat{\mathbf{e}}_1, \hat{\mathbf{e}}_2, \hat{\mathbf{e}}_3$ } :

$$\begin{pmatrix} \mathbf{a} \\ \mathbf{b} \\ \mathbf{c} \end{pmatrix}_R = \begin{pmatrix} 4.56 & 0 & 0 \\ 0 & 4.56 & 0 \\ 0 & 0 & 2.86 \end{pmatrix} \begin{pmatrix} \hat{\mathbf{e}}_1 \\ \hat{\mathbf{e}}_2 \\ \hat{\mathbf{e}}_3 \end{pmatrix} \quad (\text{A.2})$$

Space group	Structure	Element	Wyckoff Positions	Fractional Coordinates
P4 ₂ /mnm	Rutile	V	2a	(0, 0, 0) ($\frac{1}{2}$, $\frac{1}{2}$, $\frac{1}{2}$)
		O	4f	$\pm(x, y, 0)$ ($\frac{1}{2}$, $\frac{1}{2}$, $\frac{1}{2}$) $\pm(x, y, 0)$
P2 ₁ /c	M ₁	V, O(1), O(2)	4e	$\pm(x, y, z)$ ($\frac{1}{2}$, 0, 0) $\pm(x, y, \bar{z})$
C2/m	M ₂	V(1)	4e	$\pm(0, y, 0)$ ($\frac{1}{2}$, $\frac{1}{2}$, 0) $\pm(0, y, 0)$
		V(2), O(1), O(2)	4i	$\pm(x, 0, z)$ ($\frac{1}{2}$, $\frac{1}{2}$, 0) $\pm(x, 0, z)$
		O(3)	8j	$\pm(x, y, z)$ $\pm(x, \bar{y}, z)$ ($\frac{1}{2}$, $\frac{1}{2}$, 0) $\pm(x, y, z)$ ($\frac{1}{2}$, $\frac{1}{2}$, 0) $\pm(x, \bar{y}, z)$

TABLE A–1: Unit cell structure for various VO₂ crystal phases. See Table A–2 for the structural parameters (x, y, z). Fractional coordinates are coordinates in the lattice vectors basis $\{\mathbf{a}_1, \mathbf{a}_2, \mathbf{a}_3\}$

With doping [2] or uniaxial stress [3], VO₂ crystals can form in the monoclinic M2 structure which has a unit cell composed of 24 atoms.

$$\begin{pmatrix} \mathbf{a} \\ \mathbf{b} \\ \mathbf{c} \end{pmatrix}_{M2} = \begin{pmatrix} 9.066 & 0 & 0 \\ 0 & 0 & 5.797 \\ -0.149 & -4.523 & 0 \end{pmatrix} \begin{pmatrix} \hat{\mathbf{e}}_1 \\ \hat{\mathbf{e}}_2 \\ \hat{\mathbf{e}}_3 \end{pmatrix} \quad (\text{A.3})$$

Using the lattice vectors of Eq. A.2, Eq. A.1 and Eq. A.3, we can describe the various phases' unit cells using fractional coordinates. Table A–1 reports the fractional coordinates which, in combination with lattice parameters given in Eq. A.2, Eq. A.1 and Eq. A.3, enable the computations of Chapter 4.

Structure	Element	x	y	z
Rutile	V	0.0	0.0	0.0
	O	0.3001	0.3001	0.0
M1	V	0.242	0.975	0.025
	O(1)	0.10	0.21	0.20
	O(2)	0.39	0.69	0.29
M1	V(1)	0.0	0.7189	0.0
	V(2)	0.2314	0.0	0.5312
	O(1)	0.1000	0.0	0.7987
	O(2)	0.3969	0.0	0.2089
	O(3)	0.1482	0.2475	0.2942

TABLE A-2: Structural parameters for various VO₂ crystal structure

References

- [1] Volker Eyert. The metal-insulator transitions of VO₂ : A band-theoretical approach. *Ann. Phys. (Leipzig)*, 11:650–702, 2002.
- [2] M. Marezio, D. B. McWhan, J. P. Remeika, and P. D. Dernier. Structural aspects of the metal-insulator transitions in Cr-doped VO₂. *Physical Review B*, 5(7):2541–2551, 1972.
- [3] J. P. Pouget, H. Launois, J. P. D’Haenens, P. Merenda, and T. M. Rice. Electron Localization Induced by Uniaxial Stress in Pure VO₂. *Physical Review Letters*, 35(13):873–875, 1975.